

U-Th-Pb Ages Of High-Grade Metamorphism Recorded In Polymict

Eucrite Lewis Cliff (LEW) 85300

by
Andrew Paul Robertson

A thesis submitted to the Department of Earth and Atmospheric Sciences
Natural Science and Mathematics
in partial fulfillment of the requirements for the degree of

Master of Science

in Geology

Chair of Committee: Thomas Lapen

Committee Member: Minako Righter

Committee Member: Justin Simon

Committee Member: Alex Robinson

University of Houston
May 2022

Dedication

This thesis is dedicated to my wife, Taylor. Without her, none of this would have been possible

Acknowledgements

Special acknowledgements go to NASA-JSC for supplying the thin section used in this study, as well as allowing for the use of their labs. Loan Le was a huge help getting the chemical and BSE maps. Minako Richter helped to make sure all of the ICP-MS analysis went smoothly. And final thanks go to the ANSMET team for finding the meteorites for analysis.

Abstract

The inner solar system experienced an apparent increase in impact intensity almost a billion years after planet formation as predicted from Ar-Ar data of impact metamorphosed materials and crater density analyses. Evidence of this apparent increase in impact rate (the 'late heavy bombardment' or LHB) are well preserved in asteroidal materials such as the howardite-eucrite-diogenite (HED) suite of meteorites thought to originate from asteroid 4-Vesta or compositionally similar asteroidal material referred to as Vestoids.

Previous studies of the Ar-Ar and K-Ar isotope systems applied to impact melt glass, rocks, and mineral fractions, have yielded ages that are interpreted to indicate that the LHB on the HED parent body occurred between about 3.3 and 3.8 Ga. The relatively low closure temperature of ~300 C for Ar diffusion in most materials opens two interpretations of the age distributions. 1) The Ar-Ar ages reflect a period of increased bombardment. Or, 2) the Ar-Ar ages reflect waning impact intensity, where the impacts earlier than ~4.1 were largely energetic enough to fully reset the Ar-Ar system and may also be recorded in isotope systems with higher closure temperature (e.g., ~550 C for U-Pb in phosphate). With waning overall impact intensity, the Ar-Ar system would still be reset during the period between 3.3 and 3.8, but the U-Pb in phosphate ages may not be fully reset. Thus, U-Pb in phosphate ages may record impact metamorphic events that are older than Ar-Ar ages of the same specimen.

Polymict eucrite LEW 85300,46 was targeted for this analysis because the specimen is thoroughly metamorphosed, has been petrologically analyzed, and there are Ar-Ar data to compare with the phosphate age data. Three distinct phosphate ages were found in distinct clasts and matrix

within LEW 85300,46 (4479 ± 71 Ma, 4218 ± 30 Ma, 4126 ± 18 Ma). These ages correspond to a period of time between 4.5 and 4.1 Ga which predates the hypothesized LHB. The U-Pb in phosphate ages likely record intense impact metamorphism that is not typically recorded by the Ar-Ar system. Therefore, it is possible that the inner solar system did not experience a LHB, but instead experienced progressively waning impact intensity.

Table of Contents

Dedication	II
Acknowledgments	III
Abstract.....	IV
List Of Tables	VII
List Of Figures.....	VIII
1. Introduction.....	1
1.1 Solar System Formation History.....	1
1.2 Vesta Formation History.....	2
1.3 HEDs.....	4
1.3.1 Eucrites.....	5
1.3.2 Diogenites.....	5
1.3.3 Howardites.....	6
1.4 Vesta Impact History.....	7
2. Sample Description	13
2.1 History.....	13
2.2 Petrography.....	14
2.3 Thermal Data.....	14
3. Methods.....	16
3.1 Sample Acquisition And Characterization	16
3.2 Isotope Analysis.....	36
4. Results	38
4.1 U-Pb And Trace Element Data.....	38
4.2 Lithology.....	39
5. Discussion.....	45
5.1 Three Ages Of LEW 85300,46.....	45
5.2 Meaning Of Phosphate Ages.....	46
5.3 Timeline From Isotope Ages.....	46
6. Conclusion.....	49
Bibliography	50

List of Tables

Trace Element Concentrations Of Phosphates.....	39
Isotope Composition Of Phosphates.....	43

List of Figures

Differentiated Model Of 4-Vesta	3
Ternary Plot Of Breccia Classification	4
Impact Map Of 4-Vesta	7
Ar-Ar Ages Of Brecciated Basaltic Eucrites	9
Ar-Ar Ages Of Eucrites And Howardites	10
Map Of Lewis Cliff In Antarctica.....	13
LEW 85300,46 Plane Polarized Light Image	17
LEW 85300,46 Chemical Map	18
LEW 85300,46 Backscatter Electron Map	19
LEW 85300,46 Cross Polarized Light Image	20
Phosphate 1 Backscatter Electron Image	21
Phosphate 2 Backscatter Electron Image	22
Phosphate 4 Backscatter Electron Image	23
Phosphate 5 Backscatter Electron Image	24
Phosphate 6 Backscatter Electron Image	25
Phosphate 9 Backscatter Electron Image	26
Phosphate 11 Backscatter Electron Image	27
Phosphate 12 Backscatter Electron Image	28
Phosphate 13 Backscatter Electron Image	29
Phosphate 16 Backscatter Electron Image	30
Phosphate 21 Backscatter Electron Image	31
Phosphate 22 Backscatter Electron Image	32
Phosphate 24 Backscatter Electron Image	33
Phosphate 25backscatter Electron Image.....	34
Merrillite Chemical Spectra.....	35
Apatite Chemical Spectra	36
Thin Sections Before Loading Into ICP-MS	37

Reverse Isochron Of Clasts C1 And C2	40
Reverse Isochron Of Clasts C3, C4, C5 And Matrix	41
REE Graph Of Phosphates.....	44
Isotope Ages Of Different Meteorites.....	45
Impact Flux Curves For Vesta	48

1. Introduction

1.1 *Solar System Formation History*

The solar system began as a cloud of gas, ice, and dust. The earliest objects in solar system, calcium-aluminum-rich inclusions, or CAIs formed sometime between 4.567 and 4.568 Ga (Amelin et al. 2002; Bouvier et al. 2007). After enough time had passed for the gases to cool, the solar nebula began forming into a rotating disk shape (Safronov and Zvjagina 1969; Shu et al. 1987). The first pieces of dust and ice could stick together to form larger pieces (Dominik and Tielens 1997). As this process continued, larger and larger pieces of dust and ice collide with one another (Zhang et al. 2019; Pfalzner et al. 2015; Greenwood et al. 2006). Each collision allows for up to 50% of the material to build, while the other 50% ricochets off into space (Wurm et al. 2005). These collisions accrete together to form the first asteroids and planetesimals. If this process continues, then these “proto-planets” will go on to gather enough material to form a terrestrial planet, or even become the core of a gas giant (Pollack et al. 1996). If the process is cut short, due to a lack of material to continue growth, then the small planetesimal will stay an asteroid (Pollack et al. 1996). There are two proposed areas in our solar system that had less mass, and therefore couldn't support a full planet, these areas are now the asteroid belt, and the Kuiper belt (Pfalzner et al. 2015). This accretion is believed to have occurred very early on in the solar system; 4-Vesta is believed to have formed only 2Ma after the formation of CAIs (Pfalzner et al. 2015).

1.2 Vesta Formation History

Shortly after CAI formation, at 4566 Ma – 4653 Ma, 4-Vesta was accreted, melted, and differentiated into a crust, mantle, and core (Kleine et al. 2009; Misawa et al. 2005; Trinquier et al. 2008; Schiller et al. 2011). After/during accretion, Vesta was melted into a magma ocean by the decay of multiple short-lived radionuclides, such as ^{26}Al (Mandler and Elkins-Tanton 2013). The magma ocean on Vesta allowed for the complete mixing and homogenization of the Vestian interior, supported by the homogeneity in oxygen and titanium isotopes among HEDs (Zhang et al. 2012; Greenwood et al. 2013), and facilitated metal-silicate differentiation. This is evidenced by a depletion of siderophile elements in eucrites, and the correlating Hf-W fractionation, indicating that an iron-rich core formed before the crystallization of most eucrites (Richter and Drake 1997; Trinquier et al. 2008). As the magma ocean crystallized and igneous processes were operative in the lithosphere, a stratified Vesta developed (Figure 1; Mandler and Elkins-Tanton 2013). The models of Vesta's internal structure are simplified to show the different members of the major meteorite groupings that are inferred to originate from 4-Vesta: the eucrites, howardites, and diogenites (HEDs) are shown as distinct layers, when in reality they were likely formed in multiple overlapping magma chambers (Mandler and Elkins-Tanton 2013). The non-cumulate eucrite and cumulate eucrite layers represent the upper crust of Vesta. The diogenite, olivine diogenite and dunite layers represent the lower crust of Vesta. The harzburgite layer represents the mantle, and the Fe-rich core layer represents the metallic core. The black line in figure 1 represents the material that was excavated from the Rheasilvia basin during a major impact with another planetary body and reaches ~35km below the surface (Mandler and Elkins-

Tanton 2013). The “DW” and “RZ” models are based on the bulk silicate Vesta compositions from Dreibus and Wanke 1980 and Ruzicka et al. 1997, respectively. These models represent end members, and the true composition is likely somewhere in the middle.

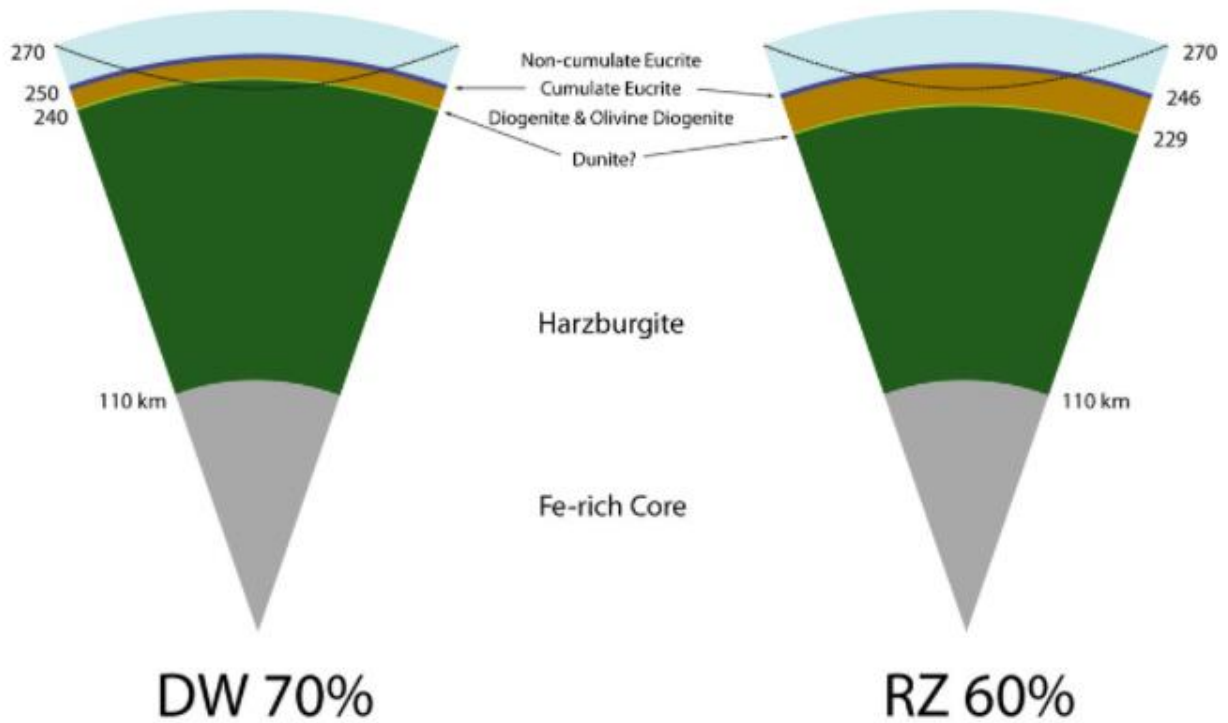


Figure 1. Differentiated models of 4-Vesta (after Mandler and Elkins-Tanton 2013). The black line represents the material that was excavated from the Rheasilvia basin during a major impact with another planetary body and reaches ~35km below the surface.

1.3 HEDs

The Howardite-Eucrite-Diogenite (HED) meteorites are a clan of achondrite meteorites that are believed to be derived from a large parent asteroid, most likely 4-Vesta (McCord et al. 1970; Mittlefehldt et al. 1998; McSween et al., 2013). The parent body of the HEDs must be a body with an extensive history of both magmatism and brecciation. Spectral data from the Dawn mission also shows similarities between the HED samples collected on Earth and the parent body 4-Vesta (Marchi et al. 2012). The abundance and petrologic diversity found in the HED suite of meteorites makes them critical for the understand of early planetary formation and evolution. Figure 2 shows the compositional relationship, and classification boundaries between howardites, eucrites, and diogenites (Mittlefehldt et al. 2013). Each peak of the triangle represents 100% of a certain endmember. Green represents polymict basaltic eucrites, blue represents polymict cumulate eucrites, red represents polymict diogenites, the green with blue stripe area represents polymict

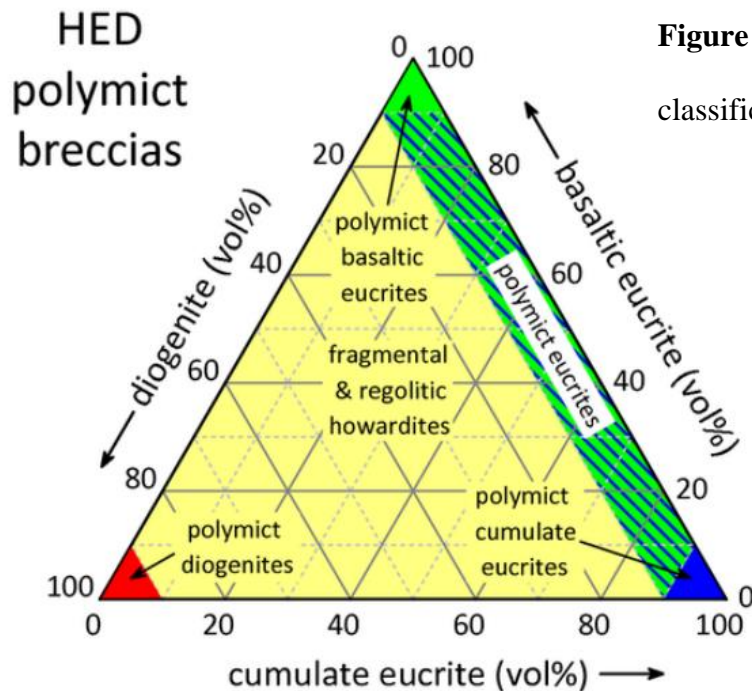


Figure 2. Ternary plot of polymict breccia classifications (Mittlefehldt et al. 2013).

eucrites, and the yellow is fragmental and regolithic howardites (Mittlefehldt et al. 2013). Specimen LEW 85300,46 would plot in the “polymict eucrite” area.

1.3.1 *Eucrites*

Eucrites originated as igneous rocks of basaltic composition that formed flows and shallow to deep intrusive bodies and are believed to represent the shallow crust of Vesta (Mittlefehldt et al. 2013). Following metal-silicate fractionation, a period of eucrite magmatism may have lasted for upwards of 100Ma, with a peak at 4552 ± 9 Ma (Misawa et al. 2005). Eucrites are mainly composed of plagioclase feldspar and low calcium-pyroxene (pigeonite), with minor phosphate, troilite, silica and ilmenite (Mittlefehldt et al. 2013). Eucrites can have a variety of igneous textures from fine-grained basaltic textures to coarse-grained cumulate textures. Eucrite meteorites can also be categorized as monomict or polymict based on the number of lithologies present. Most eucrites are brecciated and/or thermally metamorphosed, although there are a few samples which are unbrecciated at the meteorite specimen scale (McCord et al. 1970; Jérôme and Goles 1971; Cohen 2013; Mittlefehldt et al. 2013; Kennedy et al. 2019).

1.3.2 *Diogenites*

Diogenites are thought to have formed deep within 4-Vesta’s crust (Mandler and Elkins-Tanton 2013; Ruzika et al. 1997), but the timing and nature of igneous emplacements are debated. Diogenites are coarse-grained ultramafic rocks composed predominantly of orthopyroxene with variable, but typically lesser amounts of olivine, plagioclase, and/or clinopyroxene (Mittlefehldt et al. 2012). The pyroxenes in diogenites typically have higher Mg contents than pyroxene in

basaltic eucrites, but there is some compositional overlap between more evolved, noritic diogenites and the most mafic cumulate eucrites (Mittlefehldt et al. 2012). Diogenites can be categorized as orthopyroxenites, harzburgites, and rarely, dunites, based on amount of olivine present in the sample (Mittlefehldt et al. 2013). Most diogenites are heavily brecciated, shock-modified, and thermally metamorphosed (Mittlefehldt et al. 2013).

1.3.3 *Howardites*

Howardites, are different from eucrites and diogenites because they aren't a direct product of magmatism but are composed of eucrite and diogenite fragments and foreign materials that have been brecciated together (Duke 1967, Zolensky et al. 1992, Cohen 2013). Howardites can be classified as either regolithic howardites, which are the lithified remnants of the active regolith of 4 Vesta or nonregolithic howardites, which are polymict breccias (Warren et al. 2009).

Of all the different HEDs, howardites (and many polymict eucrites) record impact histories of the breccia specimen itself as well as the impact histories of the clasts. Many studies use the Ar-Ar system to identify the timing of impact events (Bogard and Garrison 2003; Cohen 2013). The abundance of HED meteorites, their petrologic diversity, and large quantities of Ar-Ar data offers an extensive record of early planetary processes that place important constraints on models of early planetary evolution, including early magmatism and later impact metamorphism, including the late heavy bombardment (LHB) (Duke 1967; Bogard and Garrison 2003; Cohen 2013; Iizuka et al. 2019; Kennedy et al. 2019; Gomes et al. 2005).

1.4 Vesta Impact History

The early solar system is characterized by periods of intense impacting (Marchi et al. 2012; Bogard and Garrison 2003; Kennedy et al. 2019). The history of this high frequency impacting was recorded on Earth but most evidence has been subsequently obscured by weathering, erosion, and plate tectonics around the planet (Marchi et al. 2012). The early solar system impacts were distributed among all planetary bodies, therefore we can still see the direct results of these impacts on other bodies such as the moon, mars, and asteroids (Marchi et al. 2012; Kennedy et al. 2019). This study focuses on meteorites thought to originate from asteroid 4-Vesta because they are numerous, are derived from the deep interior and surface, and many specimens have experienced several metamorphic episodes related to impacts. The metamorphic

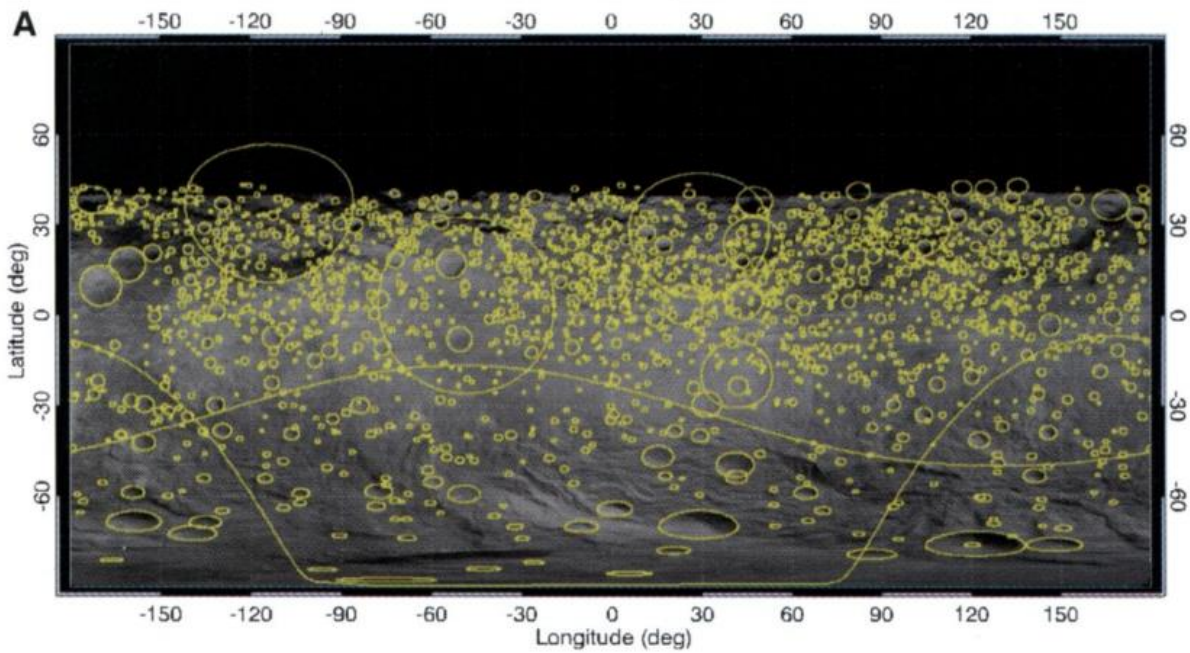


Figure 3. Impact map of 4-Vesta from the dawn mission (Marchi et al. 2012). The original Vesitan surface is gray and the different impact craters are outlined in yellow. The black area above ~40 degrees latitude was not mapped.

history of these meteorites can yield insights into the impact history of the parent body which in turn can further our understanding of impact processes across the inner solar system. The impact rates have been estimated using surface mapping of 4-Vesta during the dawn mission (Figure 3) and metamorphic and shock melting events recorded in the meteorites from 4-Vesta (Marchi et al. 2012). Figure 3 shows the southern hemisphere and part of the northern hemisphere of 4-Vesta. Individual craters are outlined in yellow, so their area can be determined easier. This map is only a 2D projection of what the true surface looks like. This causes craters near the south pole to become increasingly distorted. The largest crater on the surface of Vesta is the Rheasilvia impact crater. This crater is so large that it takes up almost the entire southern hemisphere, which is why it appears as a nearly straight line near the -40°S latitude. The cratering density and distribution allow for an assessment of the impact magnitude and rate on 4-Vesta (Marchi et al. 2012; Melosh 1996).

The temperature-time histories of the meteorites, which can be attributed to post magmatic processes such as those related to impacting, are determined by thermochronometry (e.g., Ar-Ar) in concert with petrologic analyses to determine the magnitude of heating/equilibration events (Bogard and Garrison 2003; Cohen 2013). Based on these data, there appears to be a time where there was an increase in impact events during a period between 3.3 and 3.8 Ga. This period, known as the 'Late Heavy Bombardment' (LHB) or 'Vestan cataclysm' (Cohen 2013), seems to be recorded in meteorites from 4-Vesta as well as in lunar samples. Because it is likely that the Earth-Moon system experienced similar impact histories as other inner Solar System bodies, analyses of specimens from large, differentiated asteroids can help expand the understanding of early terrestrial impact processes.

The LHB is thought to be an anomaly because a period of planetesimal impacting on such a large scale isn't expected to occur so late after initial formation (Gomes et al. 2005). Traditional

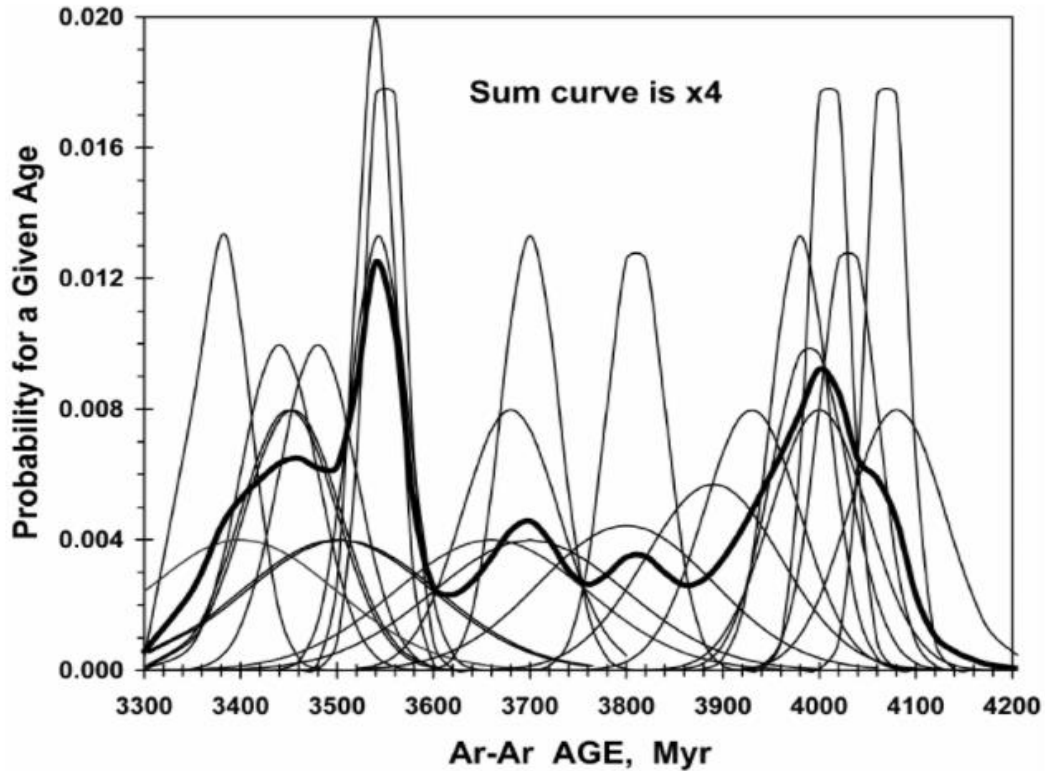


Figure 4. Ar-Ar ages of 28 brecciated basaltic eucrites. The summed age probability (heavy-line curve) has been multiplied by a factor of four (Bogard and Garrison 2003).

models of solar system formation can't account for the LHB, so one hypothesis is that the LHB was triggered by a rapid migration of the gas giants Jupiter and Saturn (Gomes et al. 2005; Tsiganis et al. 2005). This migration caused a destabilization of planetesimal orbits, which caused a mass influx of small planetary bodies into the inner solar system, while also disrupting the orbits of the asteroid belt (Gomes et al. 2005; Tsiganis et al. 2005).

Eucrites from 4-Vesta formed early after the initial formation and subsequent differentiation of 4 Vesta (Pfalzner et al. 2015; Righter and Drake 1997). U-Th-Pb in Zircon gives an initial crystallization age of eucrites at $4530\text{--}4560 \pm 5\text{Ma}$ (Iizuka et al. 2015), $4560 \pm 8\text{ Ma}$ (Liao and Hsu

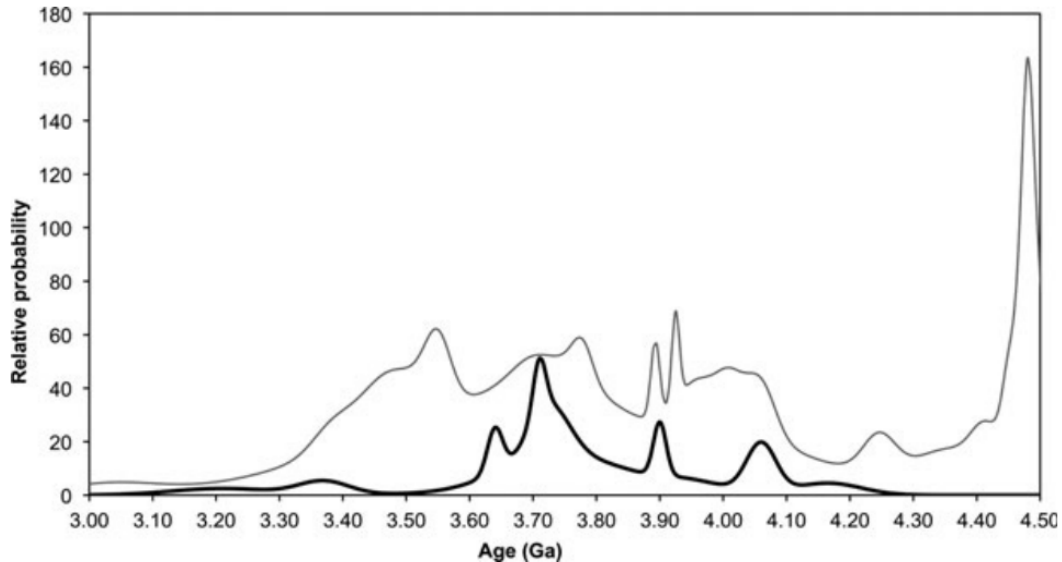


Figure 5. Ar-Ar ages of eucrites, including brecciated, unbrecciated and polymict (gray) and impact melt samples within howardites (black) (Cohen 2013). There is a noticeable spike in ages at $\sim 4.48\text{ Ga}$, followed by a sharp decrease in impacts which doesn't increase again until $\sim 4.05\text{ Ga}$.

2017) $4561 \pm 13\text{ Ma}$ (Hopkins et al. 2015). Most Eucrites have evidence of thermal metamorphism and impact brecciation after protolith formation (Kennedy et al. 2019). Past studies of Ar-Ar data show a bimodal distribution with age distributions that have peaks at $4.5\text{ -- }4.6\text{ Ga}$ and $4.1\text{ -- }3.3\text{ Ga}$ (Figure 5). The early peak is interpreted as early igneous crystallization and/or early thermal

metamorphism (Cohen 2013; Bogard and Garrison 2003). The second peak is interpreted as heating from impact events similar to that inferred from Ar-Ar data of impact metamorphosed lunar rocks (Sears et al. 1997; Bogard 1995; Cohen 2013). Using the Ar-Ar ages from Figure 4 and Figure 5, it appears that the LHB on 4 Vesta begins ~4.0 Ga followed by a peak at ~3.5Ga and finally ending ~3.3Ga (Bogard and Garrison 2003, Cohen 2013).

The impact age curves in figures 4 and 5 are based only on Ar-Ar data. The effective ‘closure temperature’ of the Ar-Ar system can be variable, depending on the temperature-time history and material properties that affect Ar diffusion. It has been shown in previous studies (e.g. Koike et al, 2020) that Ar-Ar ages are typically younger than, for example, U-Pb in phosphate. Thus, it is possible that there were thermal events of sufficient temperature and duration that the Ar-Ar system was completely reset, but not sufficient to reset the U-Pb system in phosphate or zircon which have closure temperatures of ~550°C and ~800°C, respectively (Cherniak and Watson 2001; Iizuka et al. 2015; Iizuka et al. 2019). This would mean that the Ar-Ar data could be representing later impacting, and not high energy impacts prior to 3.8-3.3 Ga. Previous studies have been done that confirm this hypothesis (e.g., Deidterich et al. 2013; Martinez et al. 2020; Tera et al. 1997; Liao and Shu 2017; Koike et al, 2020). Figure 5 (Cohen 2013) shows a period between ~4.1Ga to ~4.4 Ga where there are relatively few Ar-Ar ages before the LHB period. This means that for both the Ar-Ar and the U-Pb ages to be accurately measuring impacts there must have been an event that was energetic enough to reset both the high temperature U-Pb and Ar-Ar systems. Subsequent events that were less energetic only reset the Ar-Ar systems but did not significantly disturb the U-Pb systems in phosphate. This study aims to focus on the possibility that there are

older, intense impact ages that are recorded in the U-Pb decay system of clasts from a well characterized polymict eucrite.

2. Sample Description

2.1 History

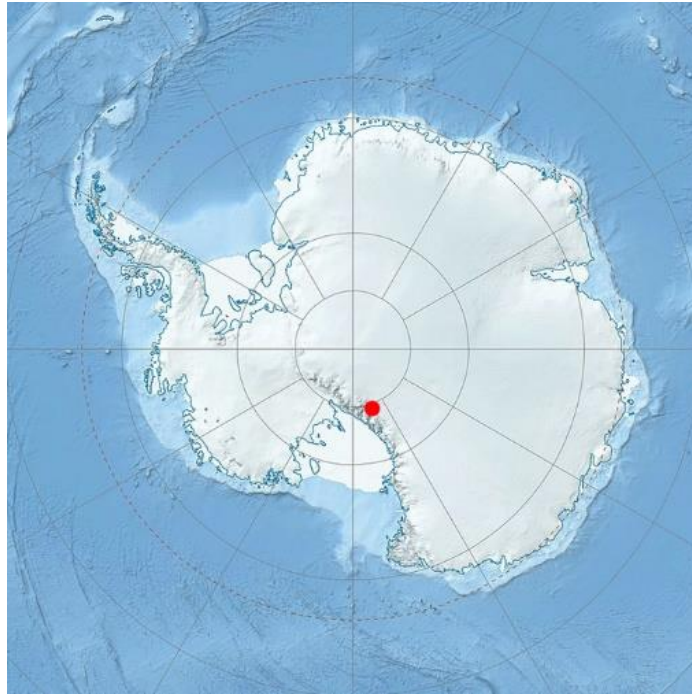


Figure 6. Map of Antarctica where the location of the Lewis Cliff meteorite was found in 1985.

This study will investigate polymict eucrites. Specifically for this study we will look at the polymict eucrite Lewis Cliff 85300 sample 46, or LEW85300-46. The “Lewis Cliff” meteorite was found near the Lewis Cliff in Antarctica in 1985 (Figure 6). This meteorite is significant because it was analyzed in great detail as part of a meteorite consortium which had the goal of better understanding the HEDs and Vesta as a whole ([Kozul and Hewins 1988a](#); [Kozul and Hewins 1988b](#); [Nyquist et al. 1990](#)).

2.2 Petrography

LEW85300 is a polymict eucrite which contains fine-grained dark matrix and numerous rock, breccia, and mineral clasts. The clasts are mainly composed of coarse to fine-grained eucrites, diogenite, and various mineral grains. Foreign materials include chondritic fragments (Zolensky et al 1992). These clasts are broken down further into three different categories, common eucritic, Mg-rich and Fe-rich (Kozul and Hewins 1988a). The common eucritic clasts contain roughly equal amounts of pigeonite and plagioclase, ilmenite and troilite are commonly disseminated throughout the clasts (Kozul and Hewins 1988a). Rare Mg-rich clasts contain higher-Mg pyroxene than the more common and more ferroan eucritic clasts (Kozul and Hewins 1988a). The matrix consists of fine-grained olivine and saponite with smaller amounts of orthopyroxene and augite (Zolensky et al. 1992). The bulk major element composition of the matrix is similar to that of chondrites. The bulk composition of the chondrite clast shows an unusual abundance pattern for lithophile, siderophile, and chalcophile elements, but is basically chondritic (Zolensky et al 1992; Kozul and Hewins 1988a). Chlorine and P X-ray maps have been taken of LEW85300 showing that Cl-rich phosphates are present in the clasts and matrix. BSE and EDS images indicate that there are zircons present large enough for in situ analysis ($>7\mu\text{m}$). Given that breccia formation is a continuous process where breccias often contain other clasts of breccia, this material likely underwent several repeated impact heating events of variable intensity (Sears et al. 1997; Pun et al. 1998).

2.3 Thermal Data

Petrologic and chronologic data show LEW 85300 records a complex thermal history. Thermoluminescence data of LEW85300 indicates both clast and matrix were heated to above 800 °C (Sears et al., 1997). Ar-Ar data of the specimen indicates a degassing event at approximately 3.5 Ga (Nyquist et al., 1990). Analyses of the Rb-Sr isotopic system in igneous-textured clasts yielded ages similar to the protolith formation ages of ~4.56Ga (Nyquist et al. 1990). Given the thermoluminescence data, it is reasonable to infer that the last recorded metamorphic event was at ~3.5 Ga and this represents the time that the specimen was assembled and lithified.

LEW 85300 also shows sensitivity to thermoluminescence, as a result of shock heating of the parent body (Kozul and Hewins 1988a; Kozul and Hewins 1988b). The Thermoluminescence data of this specimen indicates that both the clasts and the matrix were heated to the same temperature of over 800°C (Sears et al. 1997). This is significant because it means that the clasts and matrix of the Lewis Cliff meteorite were heated during final assembly.

3. Methods

3.1 Sample acquisition and characterization

The specimen studied here is LEW 85300,46 which is on loan from NASA-JSC. The section was photographed using a petrographic microscope in plane polarized, cross polarized, and reflected light (Figure 7). The sample has multiple different clasts which were identified using the optical light images, compositional Xray maps, and backscattered electron images (Figs 7-10).

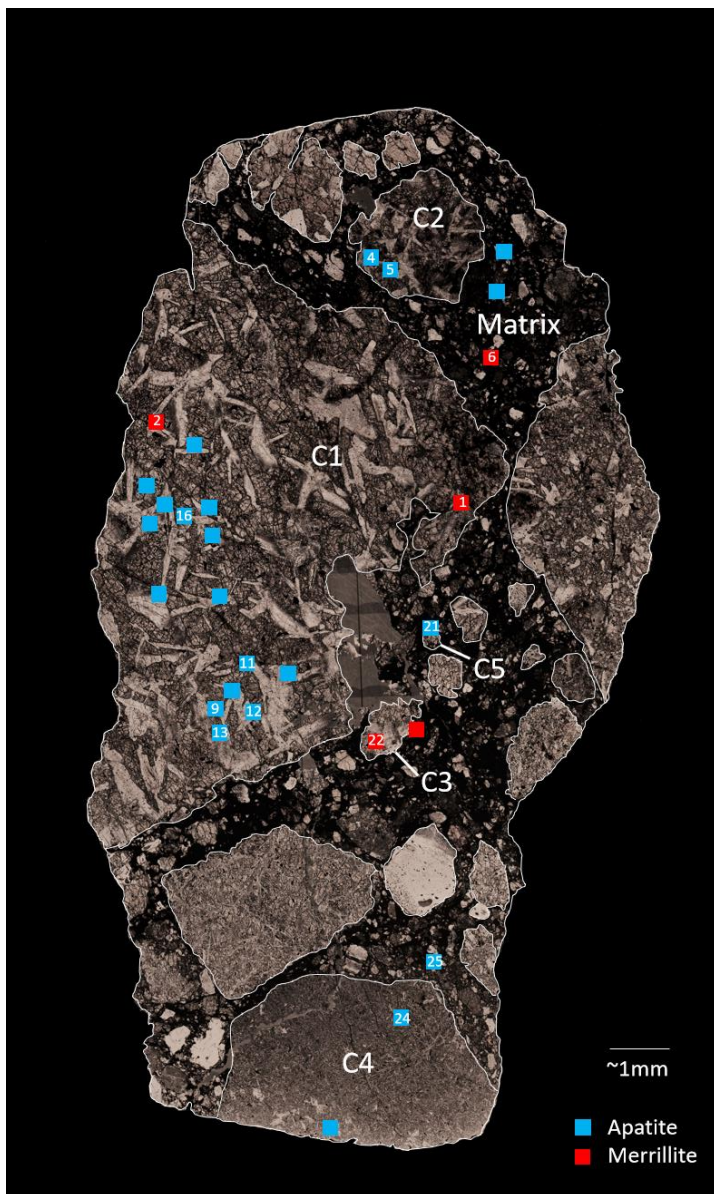


Figure 7. This is a plane polarized image of LEW 85300,46 with all the measured phosphate locations marked. The red points are the merrillite grains, and the blue points are the apatite grains. For this image the different clasts that contain phosphates have been outlined and labeled C1 (Clast 1) through C5 (Clast 5). The dark matrix has also been outlined and labeled. The phosphates that contained sufficient Pb for analysis are labeled with their specific number.

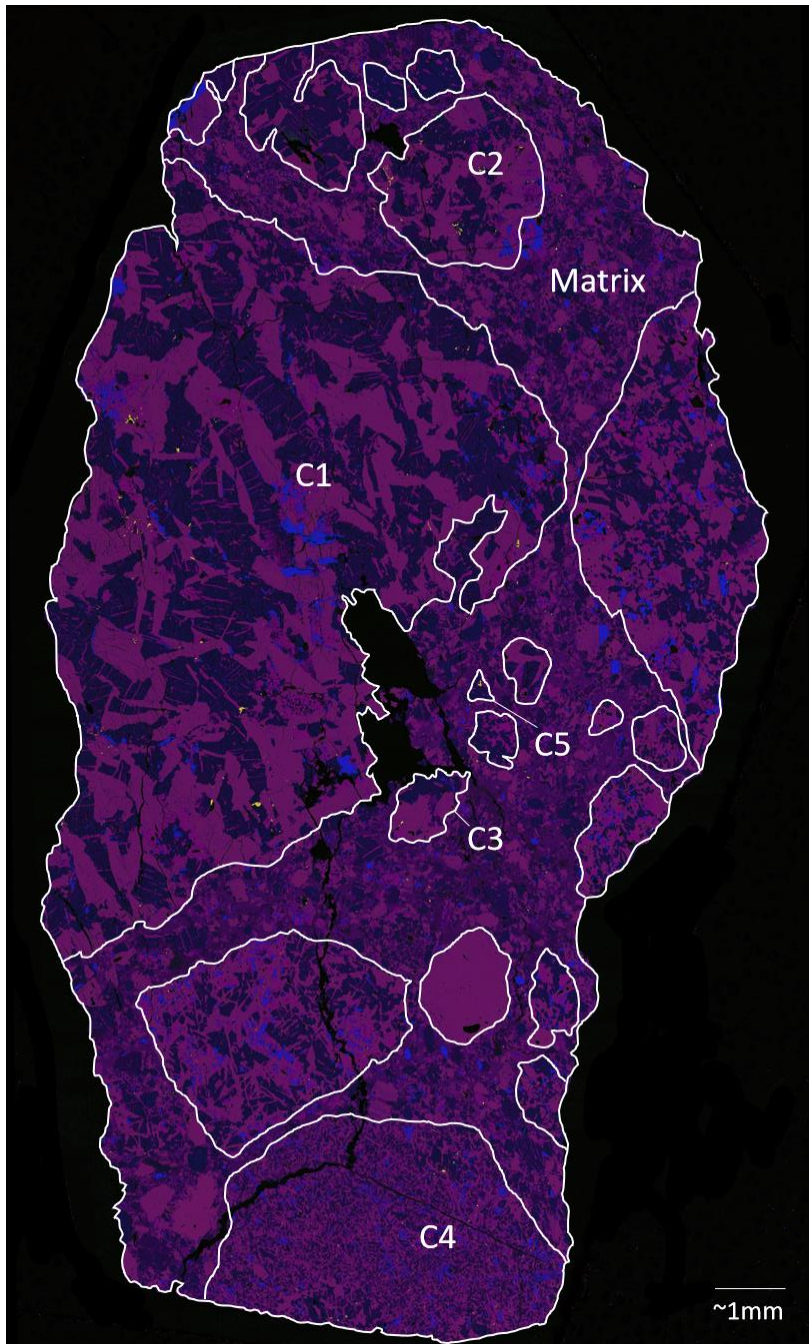


Figure 8. A chemical map taken of LEW 85300, 46. Edited in the ImageJ program so that Ca is red, P is green, and Si is blue. Under these constraints, Zircon grains will appear green, and phosphates will appear yellow. This image was edited so that clasts were outlined and labeled for easier viewing. Phosphates 1-10 were measured with the ICP-MS before the BSE and

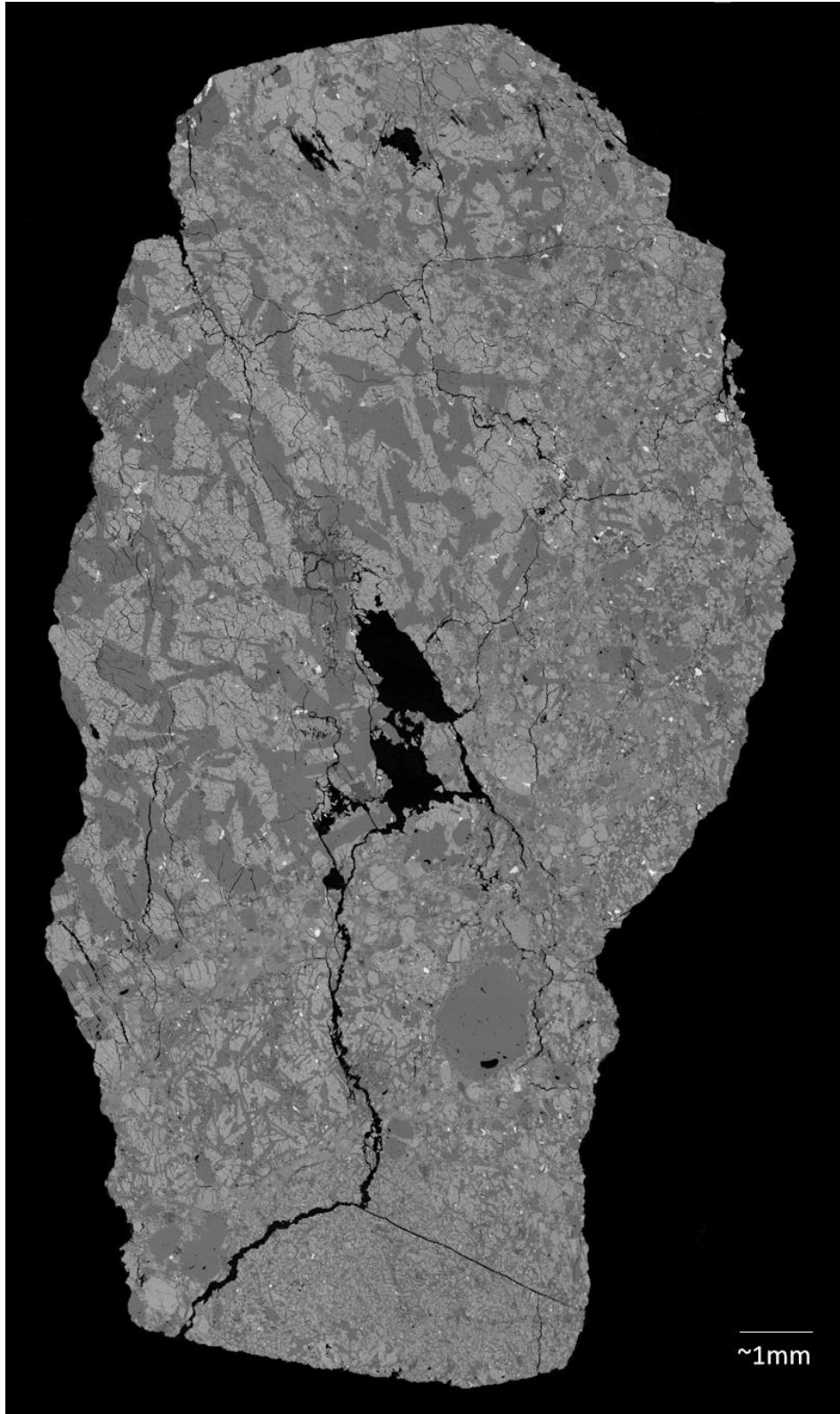


Figure 9. A backscatter electron image taken of LEW 84300, 46. This image was taken using an E-Beam at NASA – Johnson Space Center. This image is unedited.

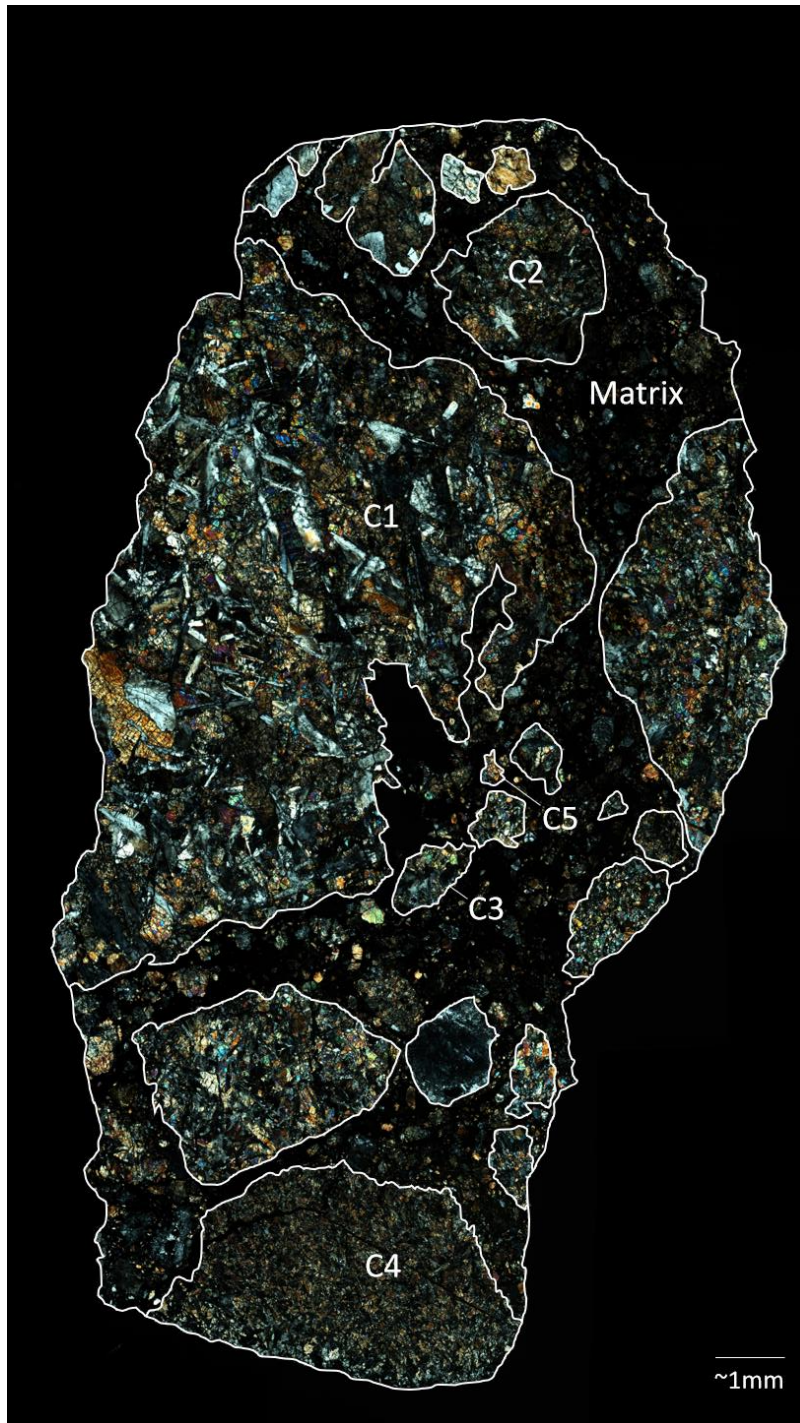


Figure 10. A cross polarized light image of LEW 85300, 46. This image was taken using an imaging microscope at the University of Houston in Houston, Texas. This image was edited so that clasts were outlined and labeled for easier viewing.

Electron Image 580

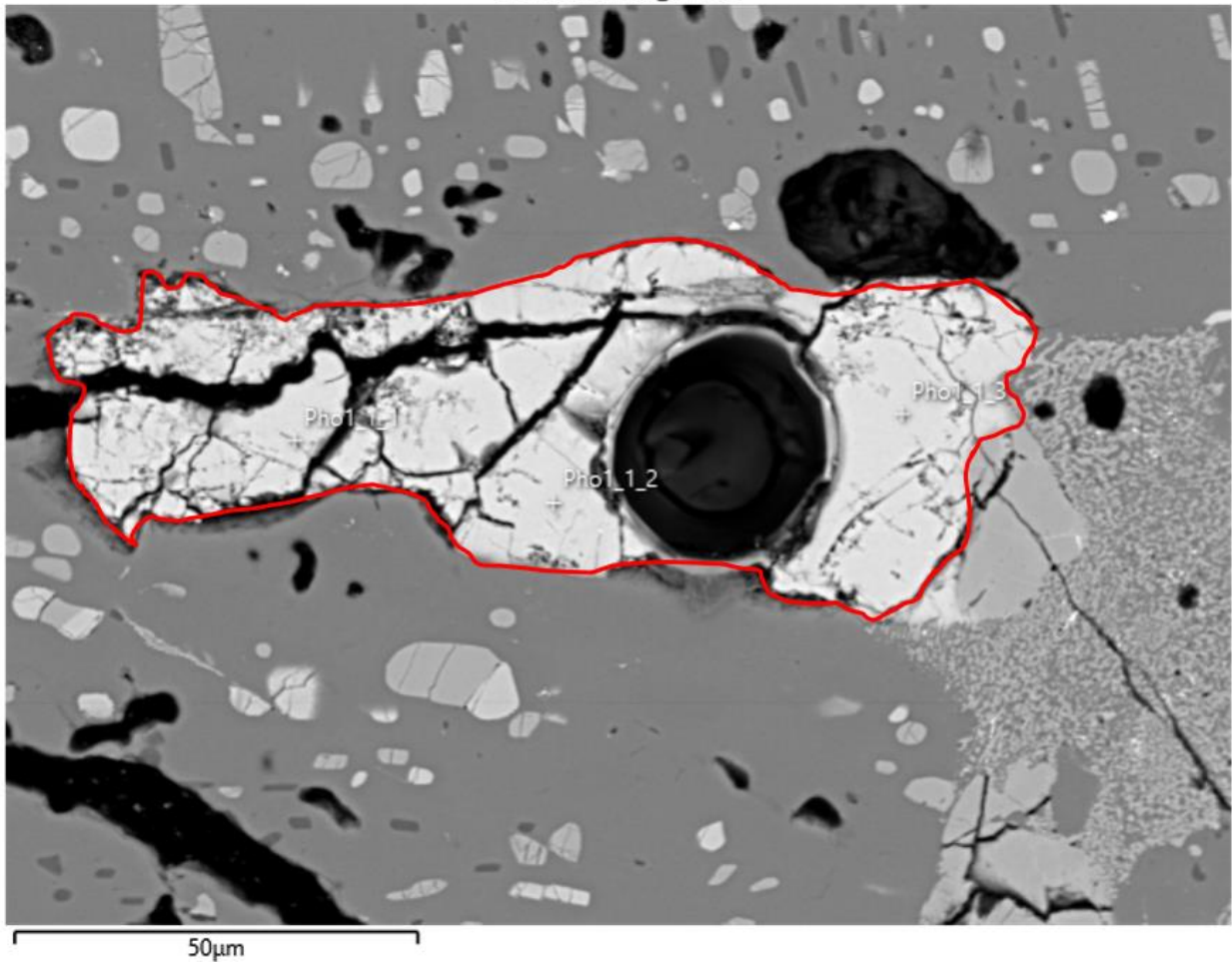


Figure 11. BSE Image of phosphate 1, outlined in red. This phosphate is a merrillite that is located within clast C1. This sample was measured on the ICP-MS prior to the BSE imaging. On this image, the three locations measured Pho1_1_1, Pho1_1_2, and Pho1_1_3 are all part of the phosphate.

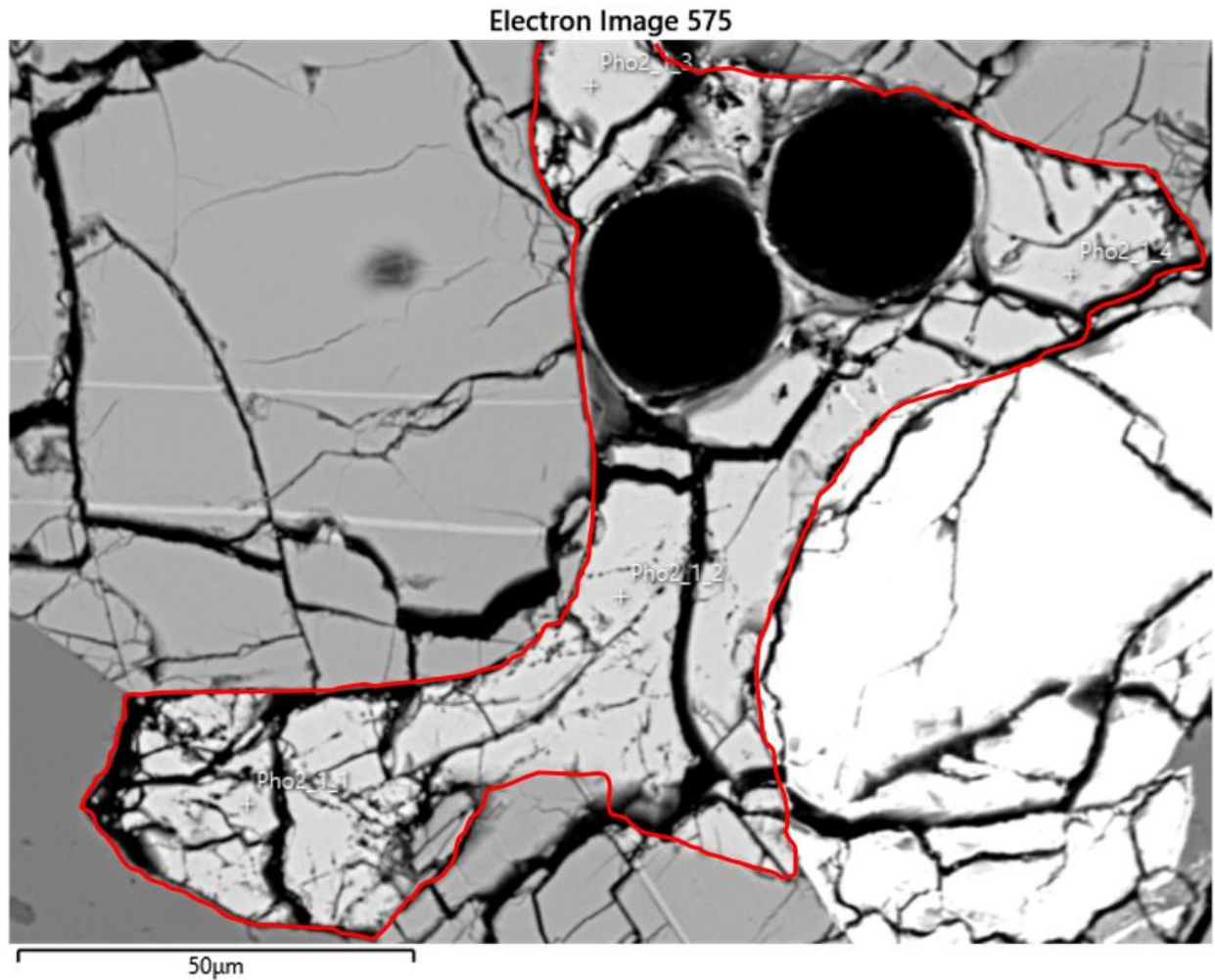


Figure 12. BSE Image of phosphate 2, outlined in red. This phosphate is a merrillite that is located within clast C1. This sample was measured twice on the ICP-MS prior to the BSE imaging. On this image, the four locations measured Pho2_1_1, Pho2_1_2, Pho2_1_3, and Pho2_1_4 are all part of the phosphate.

Electron Image 577

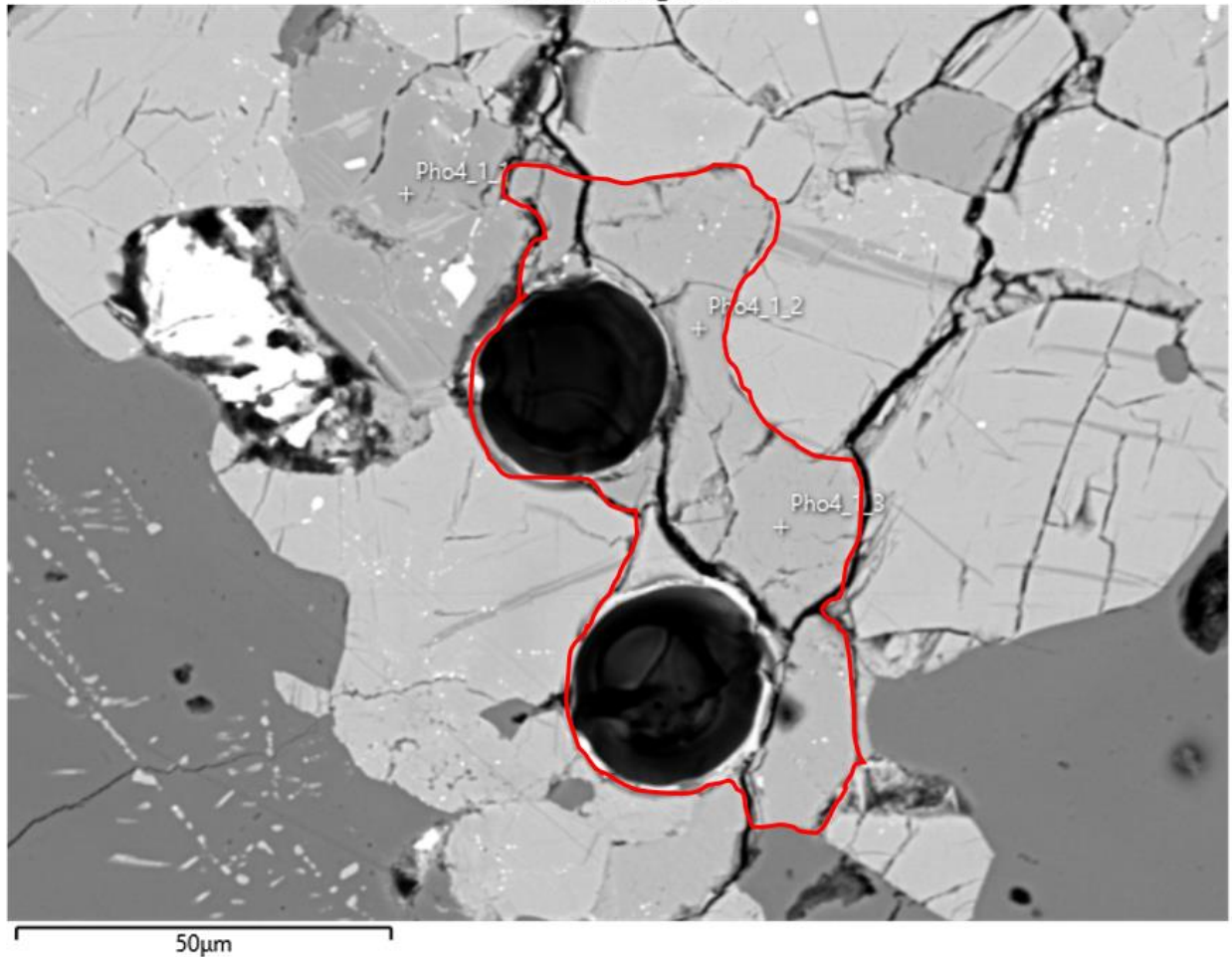


Figure 13. BSE Image of phosphate 4, outlined in red. This phosphate is an apatite that is located within clast C2. This sample was measured twice on the ICP-MS prior to the BSE imaging. On this image, location Pho4_1_1 is not a part of the phosphate, while Pho4_1_2 and Pho4_1_3 are both parts of the phosphate.

Electron Image 578

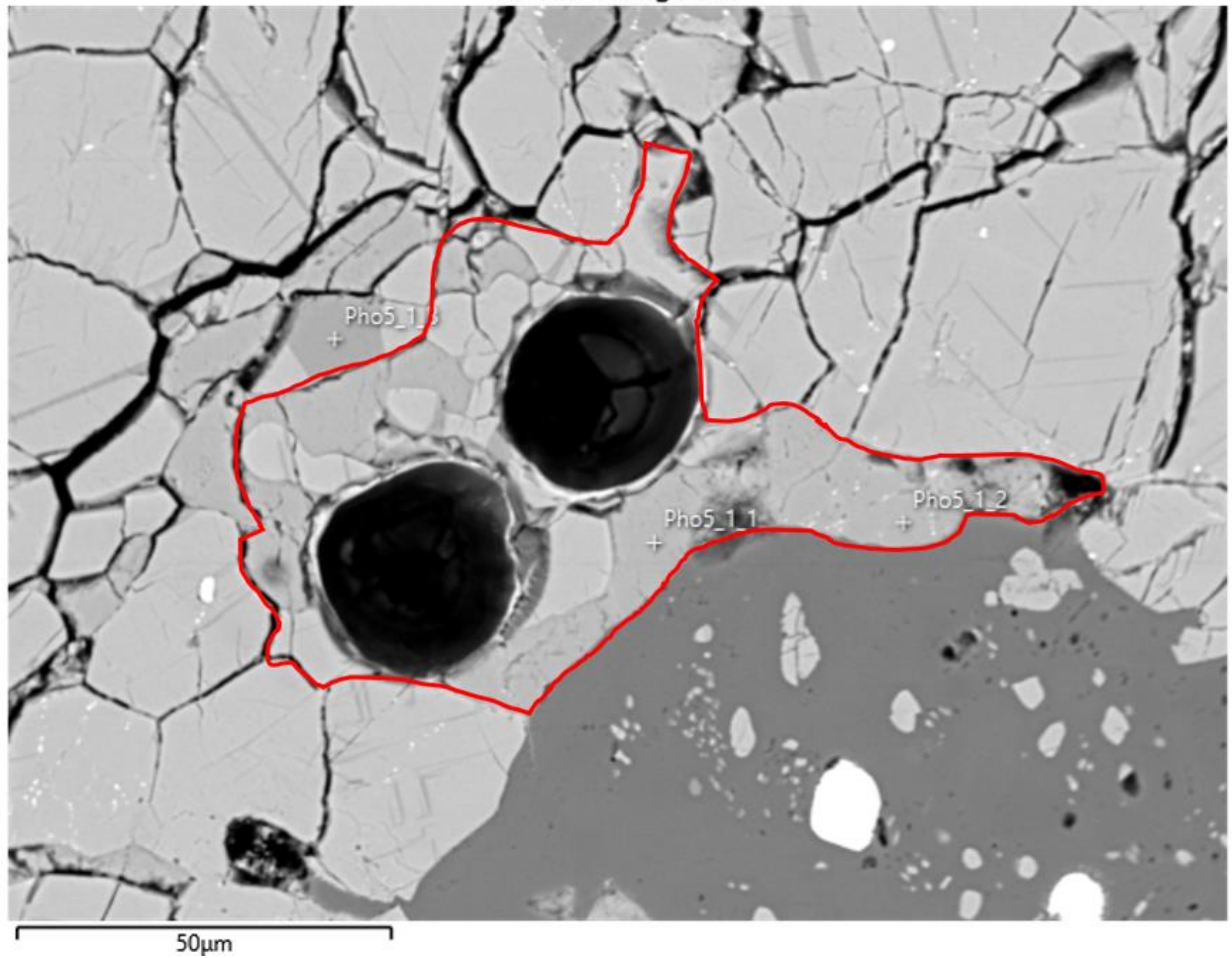


Figure 14. BSE Image of phosphate 5, outlined in red. This phosphate is an apatite that is located within clast C2. This sample was measured twice on the ICP-MS prior to the BSE imaging. On this image, locations Pho5_1_1 and Pho5_1_2 are both part of the phosphate, while location Pho5_1_3 is not a part of the phosphate.

Electron Image 579

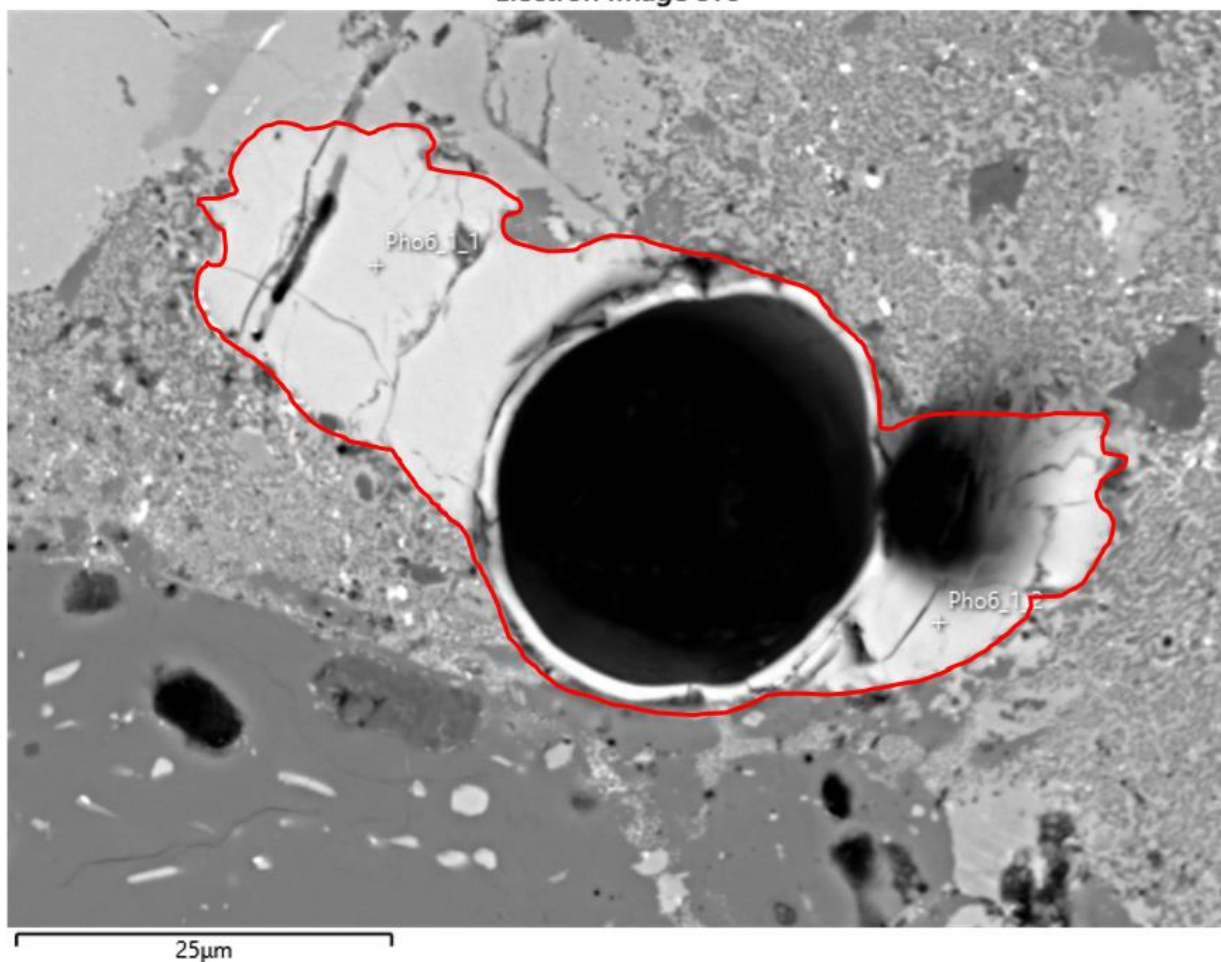


Figure 15. BSE Image of phosphate 6, outlined in red. This phosphate is a merrillite that is located within the matrix. This sample was measured on the ICP-MS prior to the BSE imaging. On this image, locations Pho6_1_1 and Pho6_1_2 are both part of the phosphate. This phosphate was one of the smallest measured, and the ICP-MS laser spot has artificially increased the diameter of the phosphate.

Electron Image 572

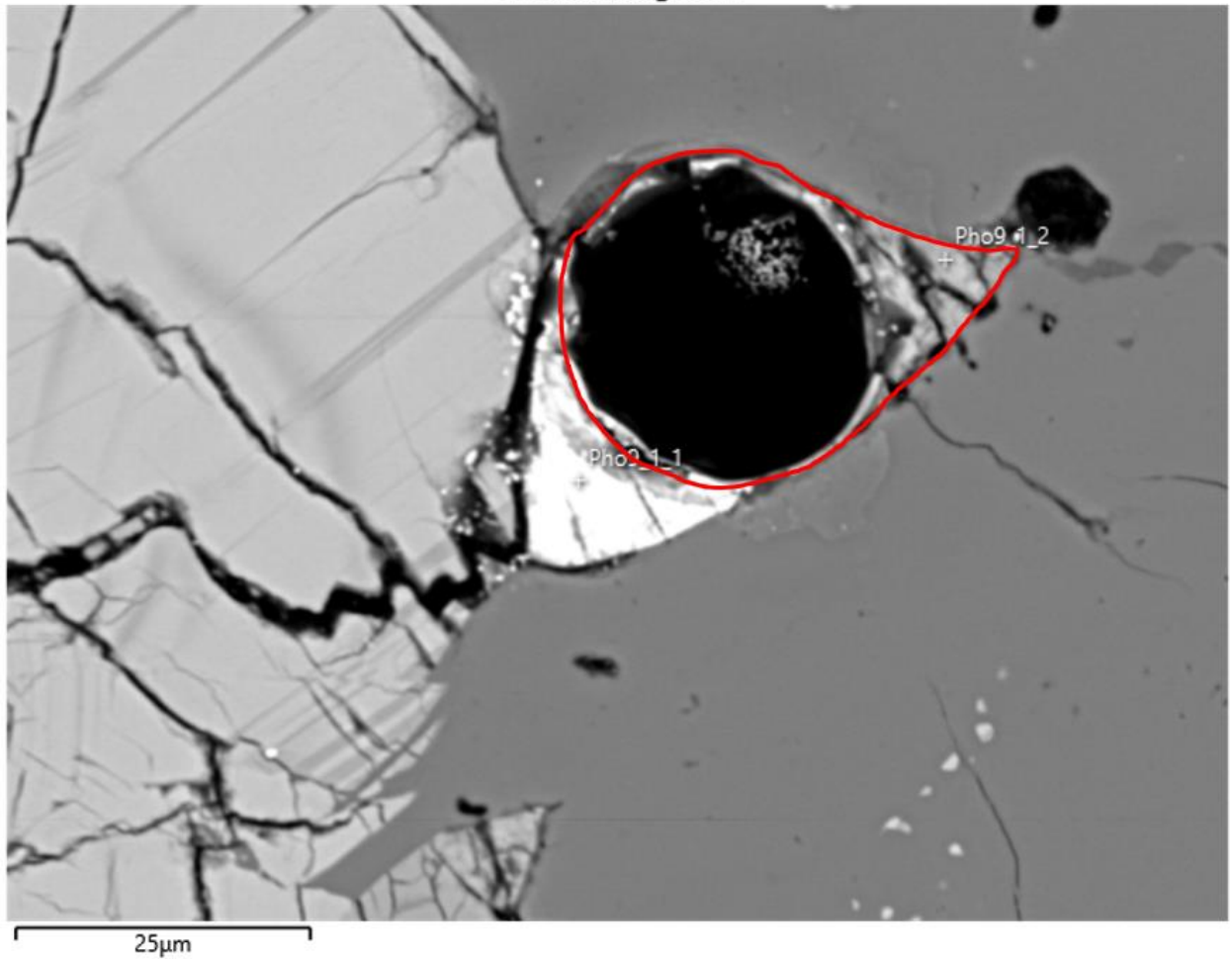


Figure 16. BSE Image of phosphate 9, outlined in red. This phosphate is an apatite that is located within clast C1. This sample was measured on the ICP-MS prior to the BSE imaging. On this image, location Pho9_1_1 is not a part of the phosphate, while location Pho9_1_2 is a part of the phosphate. This phosphate was the smallest measured, and the ICP-MS laser spot has nearly covered the phosphate in its entirety, as well as inflating its diameter.

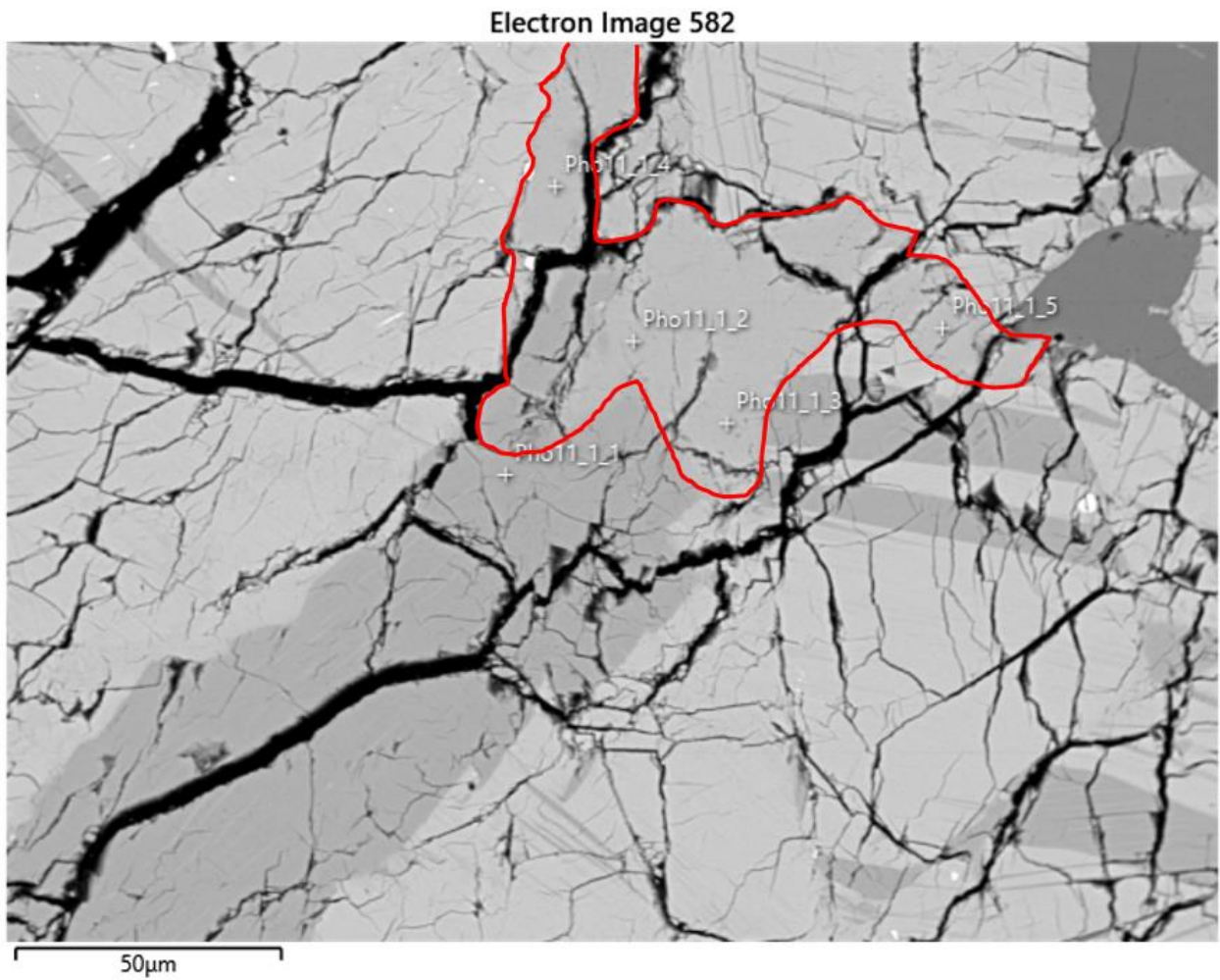


Figure 17. BSE Image of phosphate 11, outlined in red. This phosphate is an apatite that is located within clast C1. On this image, location Pho11_1_1 is not a part of the phosphate, while locations Pho11_1_2, Pho11_1_3, Pho11_1_4 and Pho11_1_5 are all parts of the phosphate.

Electron Image 583

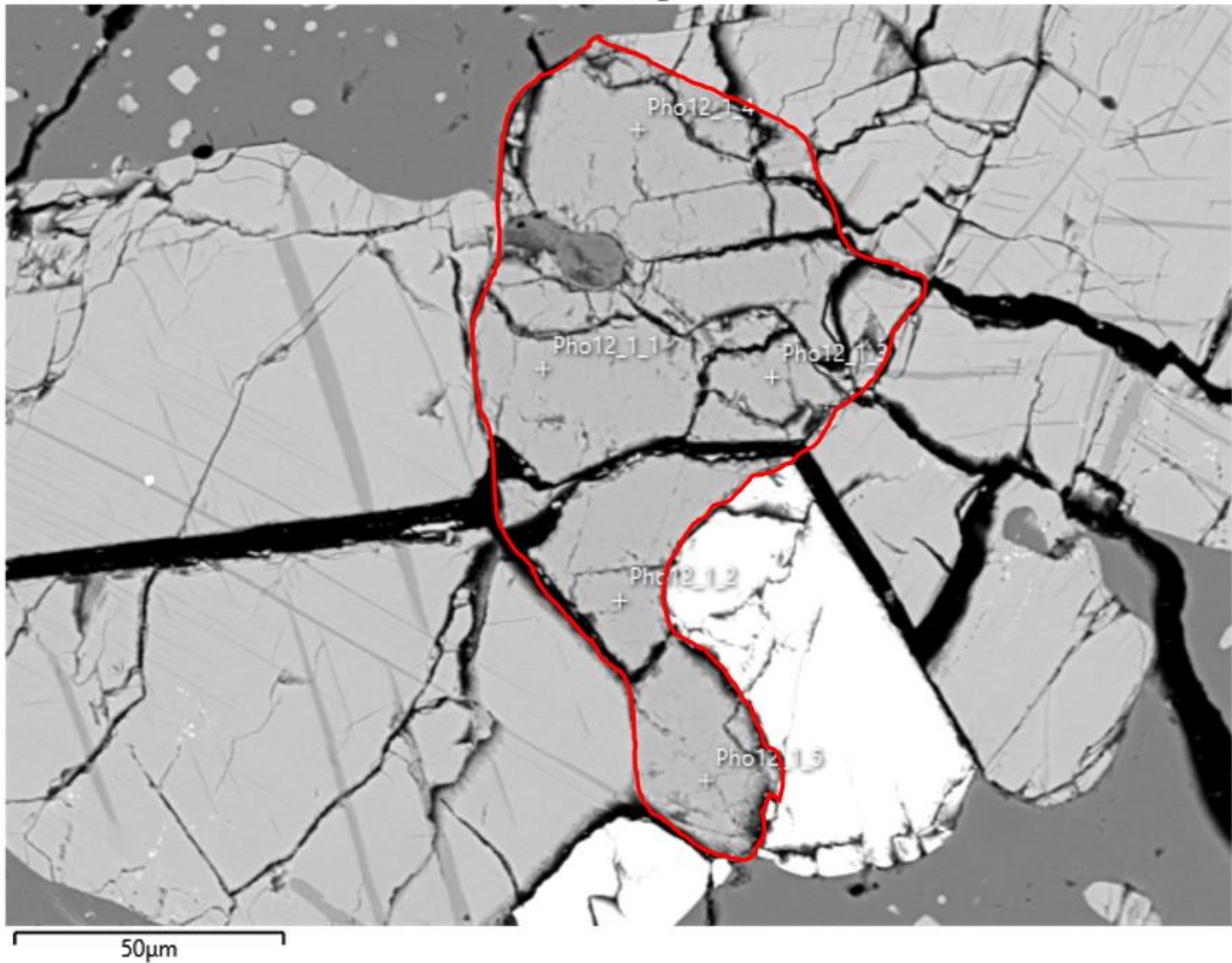


Figure 18. BSE Image of phosphate 12, outlined in red. This phosphate is an apatite that is located within clast C1. On this image, locations Pho12_1_1, Pho12_1_2, Pho12_1_3, Pho12_1_4 and Pho12_1_5 are all parts of the phosphate.

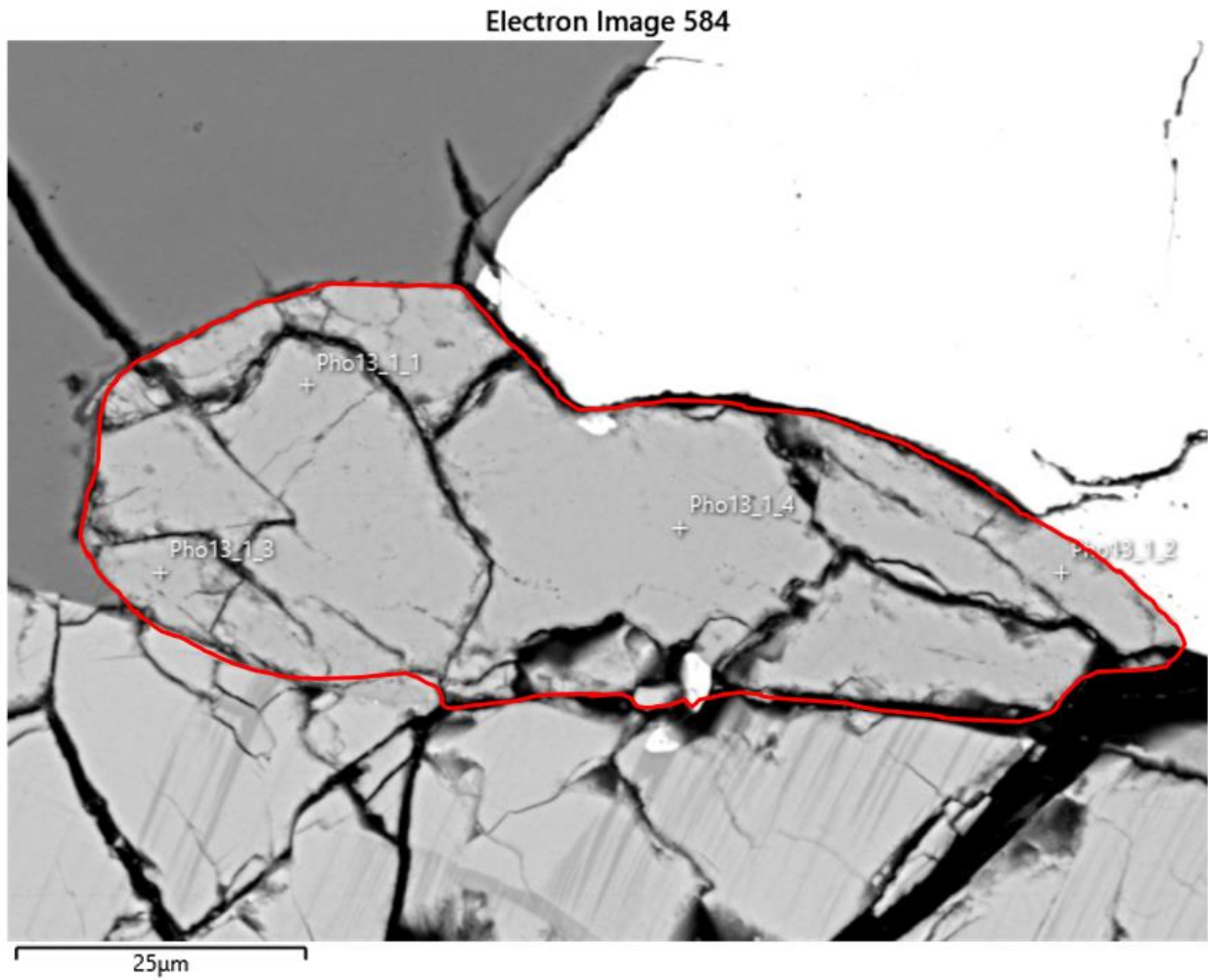


Figure 19. BSE Image of phosphate 13, outlined in red. This phosphate is an apatite that is located within clast C1. On this image, locations Pho13_1_1, Pho13_1_2, Pho13_1_3 and Pho13_1_4 are all parts of the phosphate.

Electron Image 587

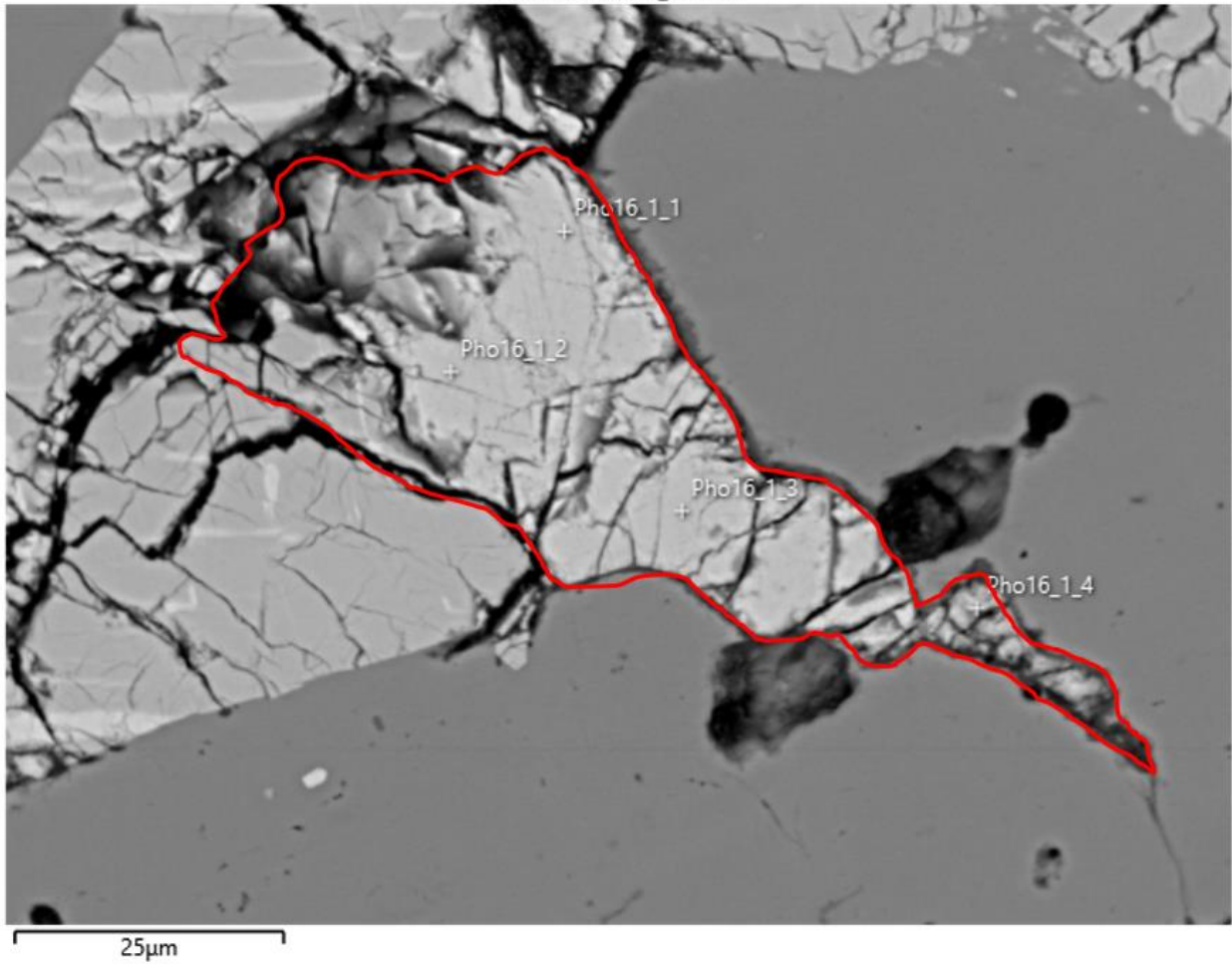


Figure 20. BSE Image of phosphate 16, outlined in red. This phosphate is an apatite that is located within clast C1. On this image, locations Pho16_1_1, Pho16_1_2, Pho16_1_3 and Pho16_1_4 are all parts of the phosphate.

Electron Image 593

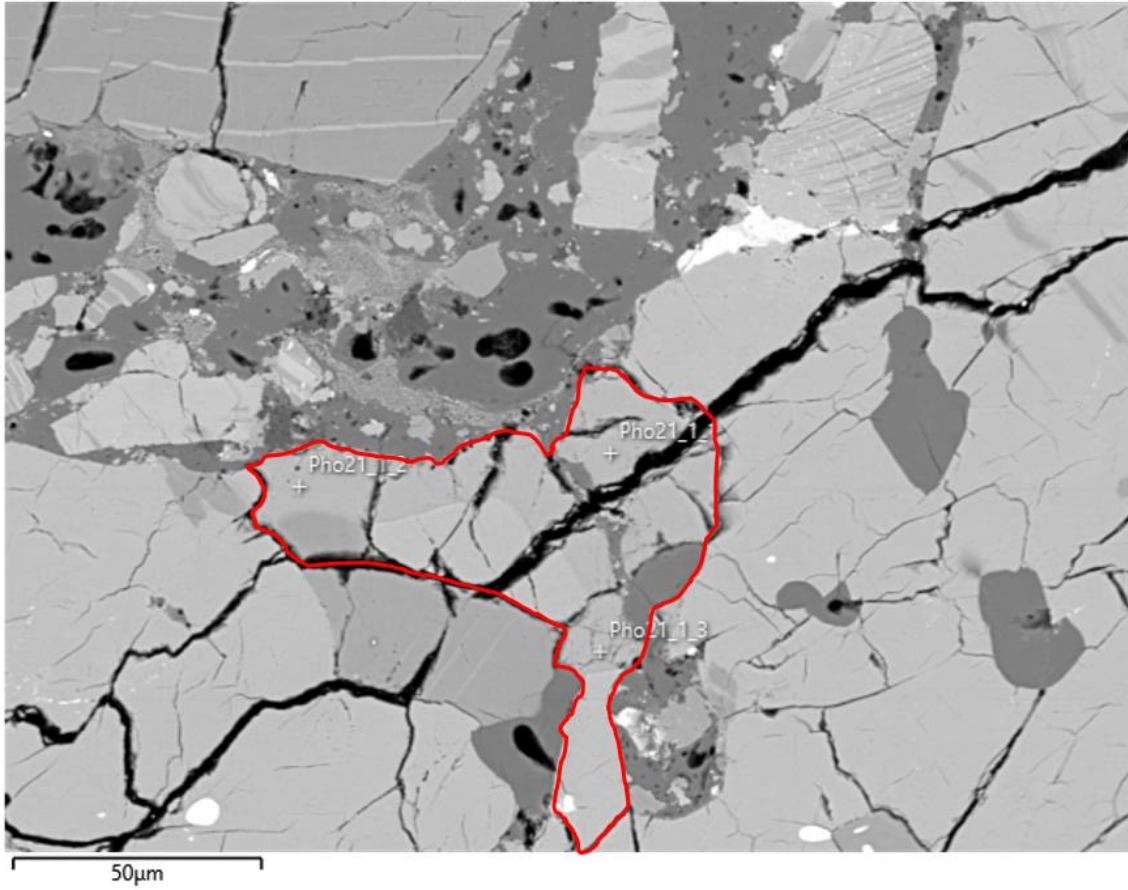


Figure 21. BSE Image of phosphate 21, outlined in red. This phosphate is an apatite that is located within clast C5. On this image, locations Pho21_1_1, Pho21_1_2 and Pho21_1_3 are all parts of the phosphate.

Electron Image 594

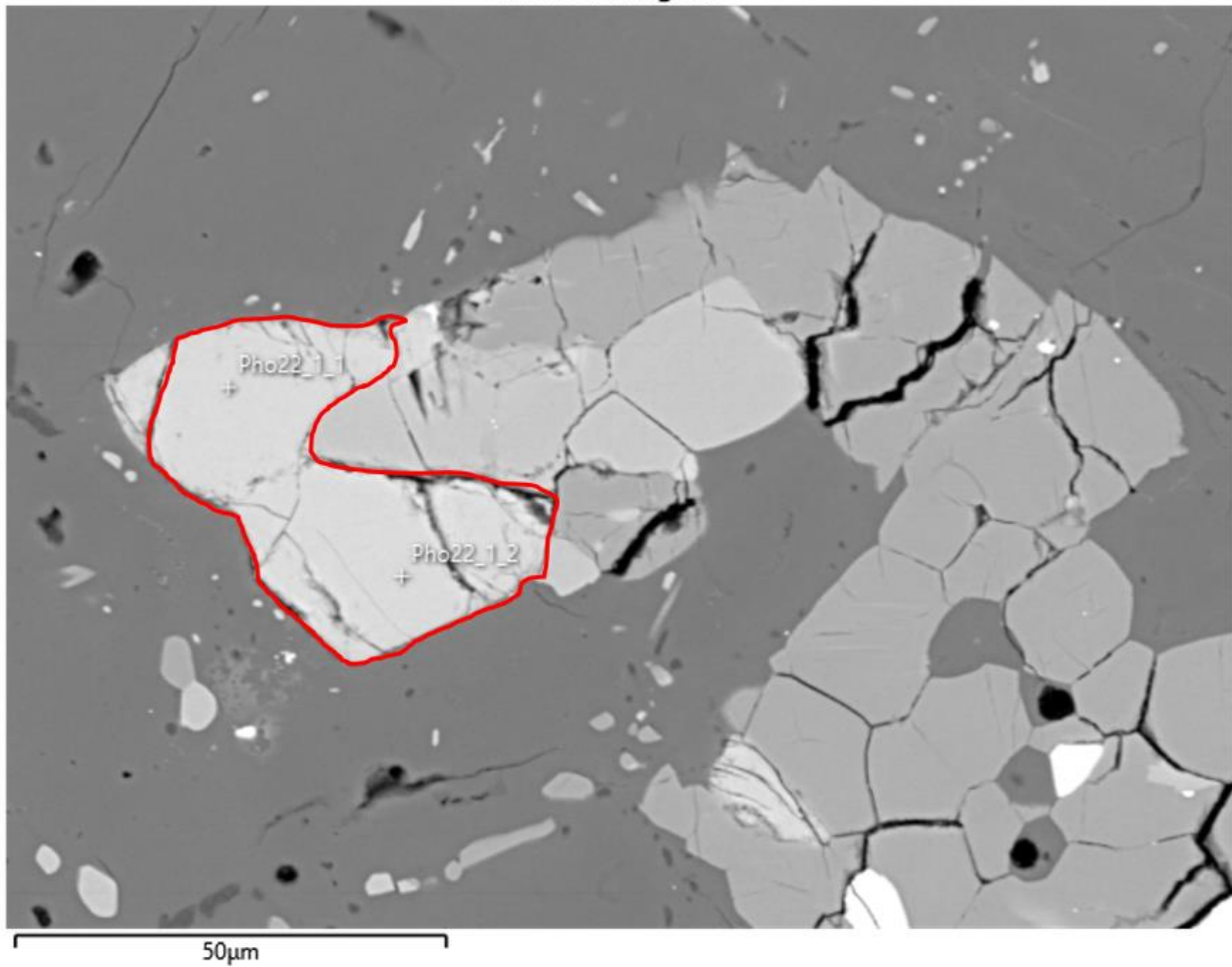


Figure 22. BSE Image of phosphate 22, outlined in red. This phosphate is a merrillite that is located within clast C3. On this image, locations Pho22_1_1 and Pho22_1_2 are both parts of the phosphate.

Electron Image 596

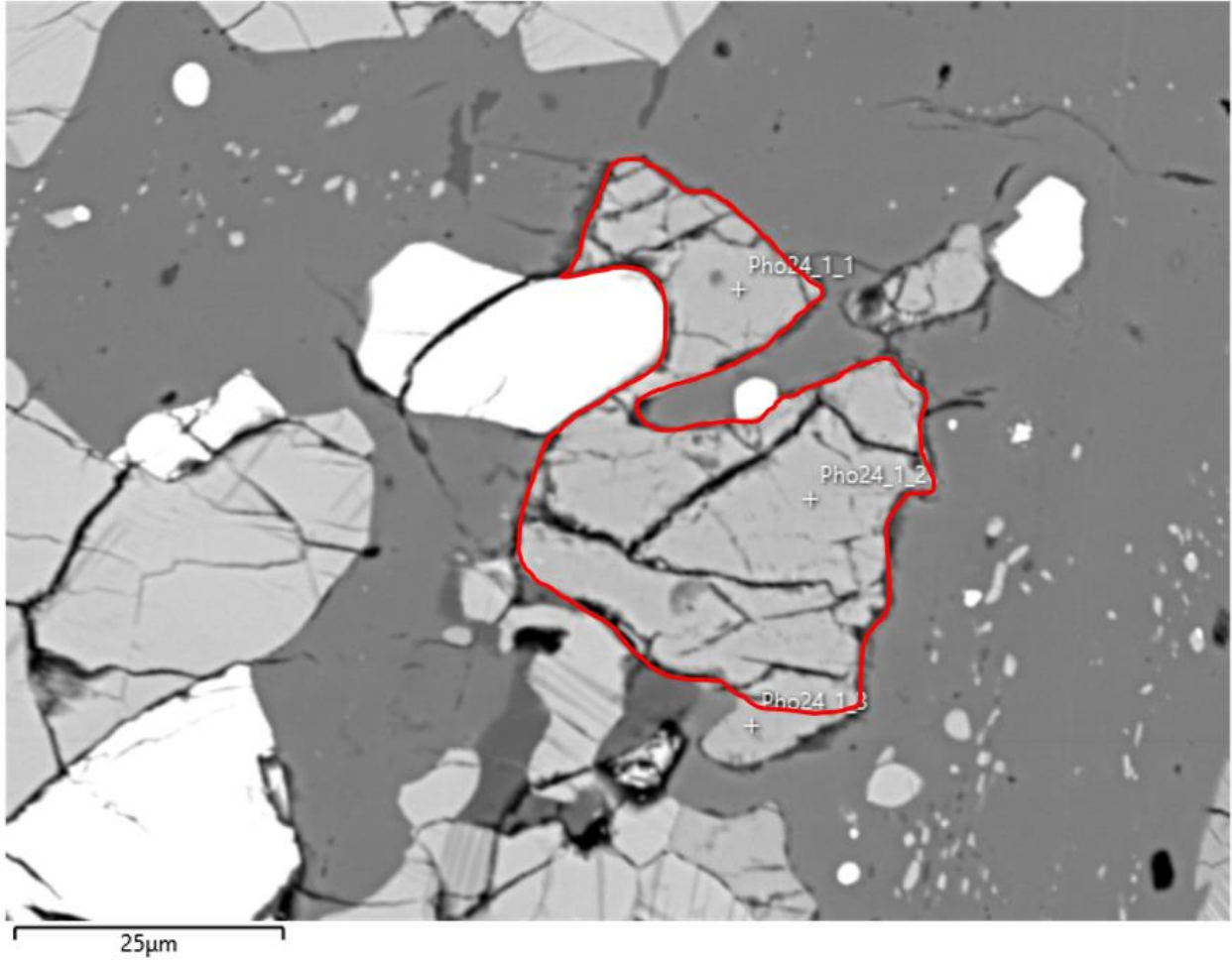


Figure 23. BSE Image of phosphate 24, outlined in red. This phosphate is an apatite that is located within clast C4. On this image, locations Pho24_1_1, Pho24_1_2 and Pho24_1_3 are all parts of the phosphate.

Electron Image 597

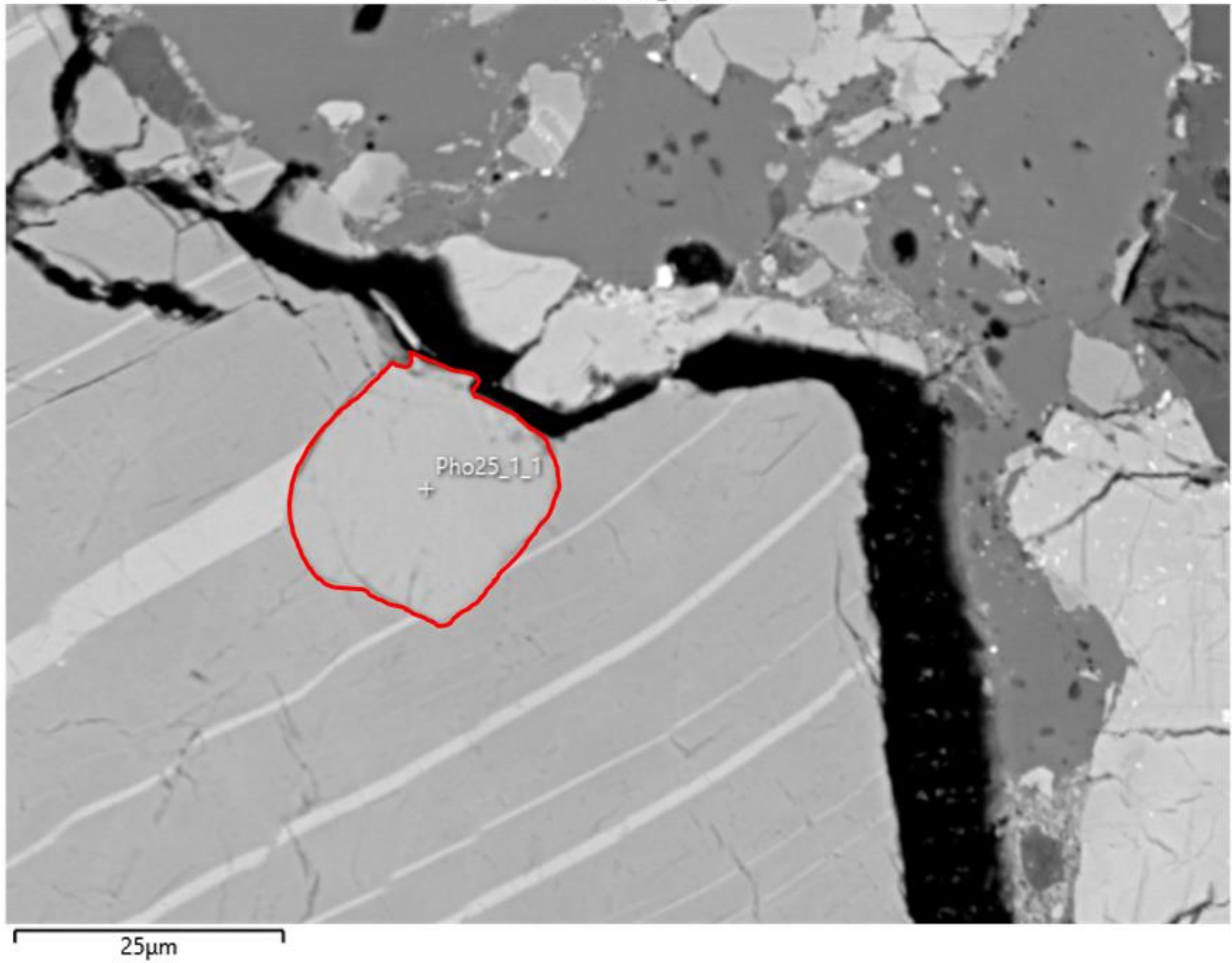


Figure 24. BSE Image of phosphate 25, outlined in red. This phosphate is an apatite that is located within the matrix. On this image, location Pho25_1_1 is in the phosphate.

Phosphates were identified in the section using an Oxford Ultimex 170 SEM at NASA-JSC. The voltage was 15kv, current 20na, 120x magnification and 100us (micron second) for dwell at a resolution of 1024. The chemical spectra were processed using the “Aztec” software. Chemical and back-scattered electron images (Figures 8 and 9, respectively) were stitched together using ImageJ. Once located, the phosphates were further imaged (Figures 11-24) and characterized as apatite ($\text{Ca}_5(\text{PO}_4)_3(\text{OH},\text{F},\text{Cl})$) and merrillite ($\text{Ca}_9\text{NaMg}(\text{PO}_4)_7$) by their chemical spectra. The two minerals are near identical in appearance, and their spectra are similar to one another. The best way to differentiate between merrillite and apatite is to look for a small peak of fluorine for apatite and a similarly small peak of magnesium for merrillite. Examples of these spectra are shown in Figures 25 and 26.

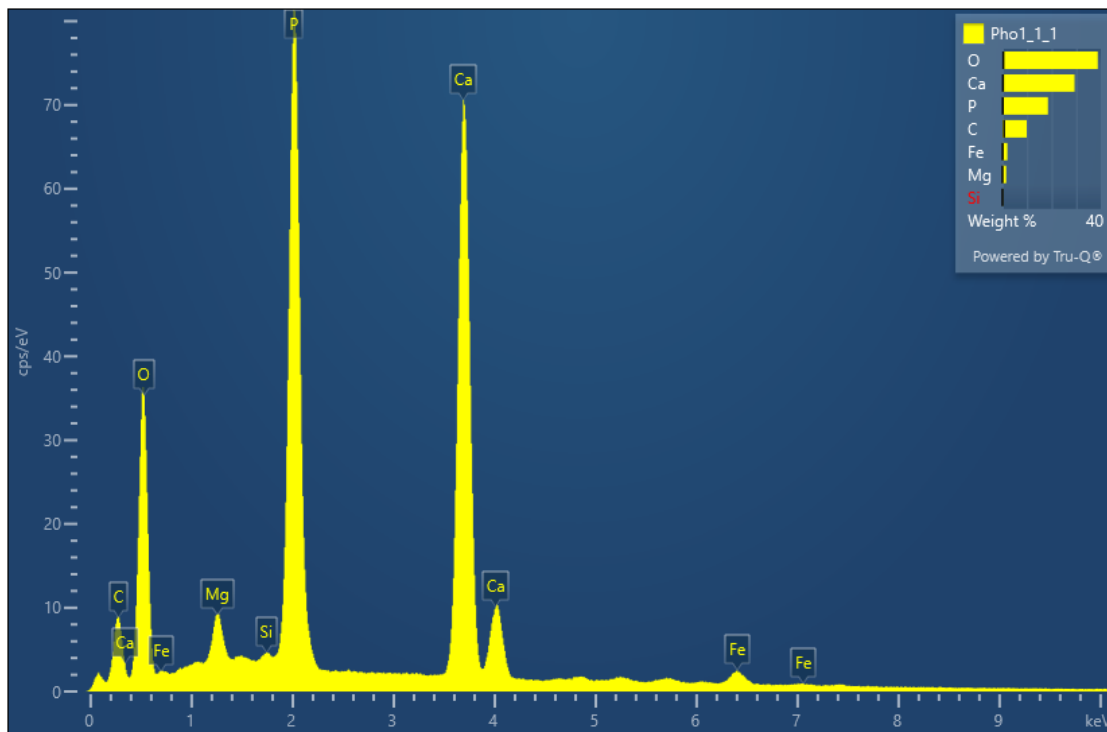


Figure 25. This is an example of a chemical spectra from a Merrillite grain (Phosphate #1)

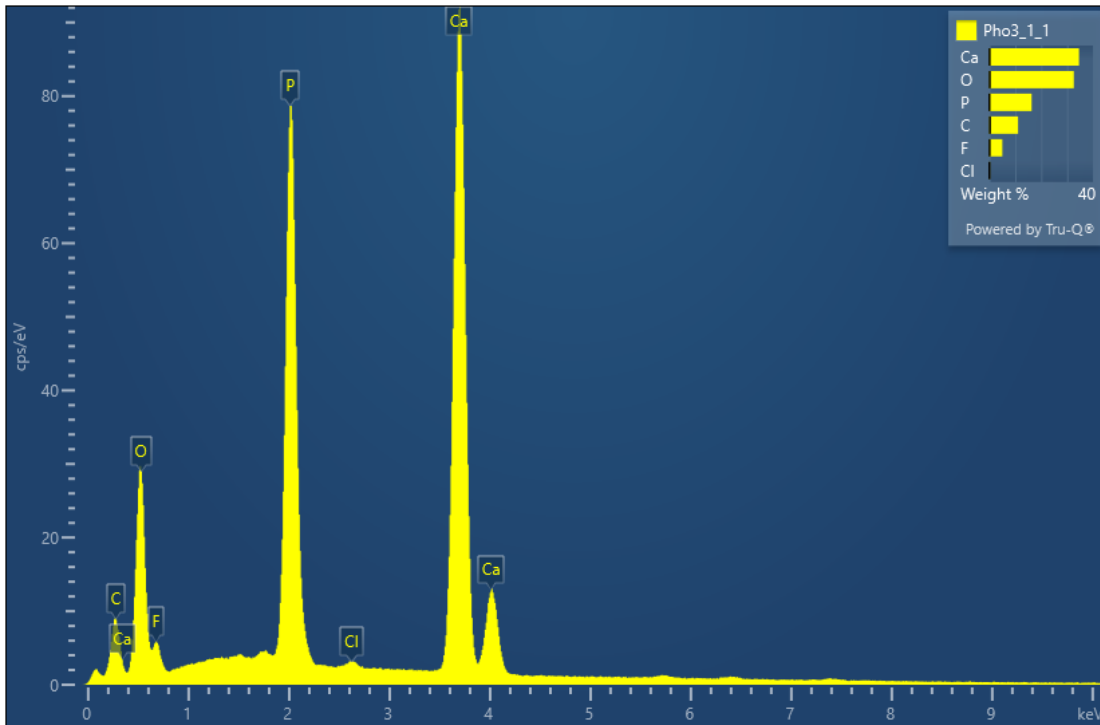


Figure 26. This is an example of a chemical spectra from an apatite grain (Phosphate #3).

3.2 Isotope analysis

In-situ U-Th-Pb isotopic analysis was carried out using a Photon Machines *Excite* (Figure 27) coupled to a Jena PlasmaQuant quadrupole ICP-MS at University of Houston. The laser analyses used 25 μm spot sizes with repetition rate of 10 Hz and an energy output of 11.28 J/cm². The laser was set to 100% power. Individual spot analyses are 60 seconds in length and are split into three parts with each lasting approximately 20 seconds: background measurements, ablation and wash-out. The Bear Lake apatite (956 ± 18 Ma) (Thompson et al. 2012) was used as the internal calibration standard, and the Yates Mine apatite (913 ± 7 Ma) (Barfod et al. 2005) and the

Madagascar apatite (486.58 ± 0.85 Ma) as the external standards for U-Pb and Th-Pb fractionation. Instrumental fractionation of Pb isotopes was monitored with NIST 612 glass. A total of 36 spots were measured across 28 different phosphates. Due to many phosphates being small and the variable signal durations, this study only focusses on the Pb isotopes, as the U-Pb systematics are unreliable due to variable U/Pb fractionations between samples and standards. Trace element data were collected for analyses simultaneously with the Pb isotope data. Analytical details and data reduction techniques are reported in (Shaulis et al. 2017; Sarafian et al. 2017).



Figure 27. Samples before loading into the ICP-MS. The bottom sample is LEW 85300-46, the middle sample are the standards that were used, and the top sample was for another study, unrelated to this paper.

4. Results

4.1 U-Pb and trace element data

A total of 36 analyses were made on 28 phosphate grains. These grains range in size from 25 -100 μm in diameter and occur in both the matrix (Figure 12, Figure 15, Figure 24) and within clasts (Figures 11-23). Due to the small grain sizes and irregular mineral boundaries, many phosphate analyses represented mixtures of phosphate and other phases. Of the phosphates found, 23 were located within igneous clasts and 5 were located in the matrix. Only 14 phosphates yielded useable data, 12 were located within clasts and 2 were located within the matrix. All Pb data are listed in Table 1. The analyses used to calculate an age show evidence of a small common Pb component. Therefore, a $^{207}\text{Pb}/^{206}\text{Pb} - ^{204}\text{Pb}/^{206}\text{Pb}$ isochron approach is used to calculate radiogenic $^{207}\text{Pb}/^{206}\text{Pb}$ ratios and an age. All dates were calculated with IsoPlot 3.76. The analyses of clast C1 and C2 yield an intercept $^{207}\text{Pb}/^{206}\text{Pb}$ ratio of 0.4627 ± 0.0055 and corresponding Pb-Pb age of 4126 ± 18 Ma (2SD; Figure 28). The analyses of clast C3, C5, and the matrix yield an intercept $^{207}\text{Pb}/^{206}\text{Pb}$ ratio of 0.4922 ± 0.010 and corresponding Pb-Pb age of 4218 ± 30 Ma (2SD; Figure 29). Clast C4 was given its own age, as it didn't fit into the other age calculations. Clast C4 only contains a single phosphate, phosphate 24 (Figure 23). The calculated Pb-Pb age for this clast is 4479 ± 71 Ma.

Trace element concentration data are listed in Table 2 and plotted in Figure 30. Trace element data were collected simultaneously with the U-Pb data. The internal standard used was ^{43}Ca and the data were processed with the computer program GLITTER. Most apatite data are

similar with the exception of grains from clasts C4 and C5, which differ in age and texture from clasts C1 and C2.

Spot ID	$^{204}\text{Pb}/^{206}\text{Pb}$	2% SD	$^{207}\text{Pb}/^{206}\text{Pb}$	2% SD	rho	Location	Type
Phos 1	2.09E-02	90	0.5477	14	0.0694	C1	Merrillite
Phos 2a	4.47E-02	42	0.6954	5.8	0.1059	C1	Merrillite
Phos 2b	3.12E-02	84	0.6619	13	0.0691	C1	Merrillite
Phos 4a	4.68E-03	31	0.5156	4.7	0.1341	C2	Apatite
Phos 4b	8.74E-03	77	0.5503	9.4	0.0767	C2	Apatite
Phos 5a	1.79E-03	41	0.4753	1.6	0.0242	C2	Apatite
Phos 5b	8.21E-04	88	0.4724	1.7	0.0070	C2	Apatite
Phos 6	2.33E-02	47	0.5937	5.2	0.0604	M	Merrillite
Phos 9	9.73E-05	131	0.4564	1.9	0.0048	C1	Apatite
Phos 11	1.35E-03	53	0.4680	4.0	0.0408	C1	Apatite
Phos 12a	9.23E-04	99	0.4647	5.6	0.0248	C1	Apatite
Phos 12b	-1.03E-03	186	0.4697	6.3	0.0043	C1	Apatite
Phos 13	-1.52E-04	443	0.4733	4.9	0.0035	C1	Apatite
Phos 16	2.46E-03	57	0.4812	4.0	0.1414	C1	Apatite
Phos 21	1.39E-04	434	0.5049	4.4	0.0067	C5	Apatite
Phos 22	3.29E-03	72	0.5158	4.2	0.0275	C3	Merrillite
Phos 24	1.97E-03	94	0.5882	5.0	0.0947	C4	Apatite
Phos 25	2.32E-04	159	0.4880	2.4	0.0009	M	Apatite

Table 1. Measured isotopic compositions of all the phosphates that contained significant enough Pb to measure. The rho column contains the error correlation calculated using equations in (Schmitz and Schoene 2007).

4.2 Lithology

This study didn't include any new petrology of LEW 85300,46. Therefore the specific lithologies of the different clasts are unknown. Phosphates that are located within the same clast are related and are given the same color coordination in the figures and tables. Specific clasts do

seem to originate from the same material. For example, clasts C1 and C2 both have the same coarse grained, gabbroic texture. They are similar in all images, the plane polarized light (Figure 7), the cross-polarized light (Figure 10), the backscatter electron image (Figure 9), and the chemical map (Figure 8). Clasts C1 and C2 also have very similar ages; figure 28 shows a reverse Pb-Pb isochron with all the points from clasts C1 and C2. The ages that were found in

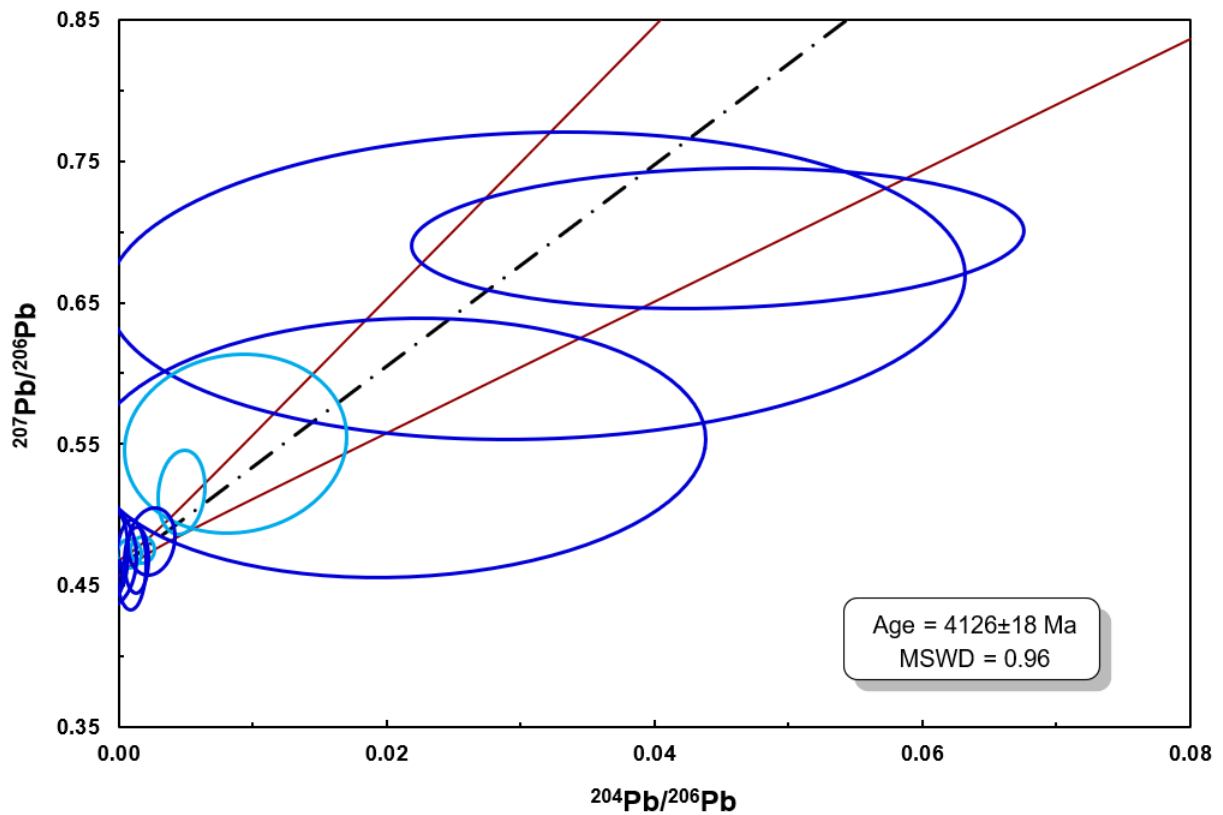


Figure 28. A reverse Pb/Pb isochron of phosphates located in clasts 1 (dark blue) and 2 (light blue). All data from clast C1 and C2 yield indistinguishable $^{207}\text{Pb}/^{206}\text{Pb}$ intercepts. Thus, the data were combined. The $^{207}\text{Pb}/^{206}\text{Pb}$ intercept = 0.4627 ± 0.0055 , age = 4126 ± 18 Ma.

these clasts have indistinguishable $^{207}\text{Pb}/^{206}\text{Pb}$ intercepts. Clasts C3, C5, and the Matrix all have a similar texture and age to one another. Clasts C3 and C5 are both small clasts that are completely surrounded by matrix. Figure 29 shows a reverse Pb-Pb isochron with the points from clasts C3, C4, C5, and matrix. Clast C4, while shown on the isochron, was not used for the regression calculation shown in figure 29. Clasts C3, C5 and matrix have some variations in their $^{207}\text{Pb}/^{206}\text{Pb}$ intercepts, but still have another strong MSWD of 1.2. Clast C4 is different in both

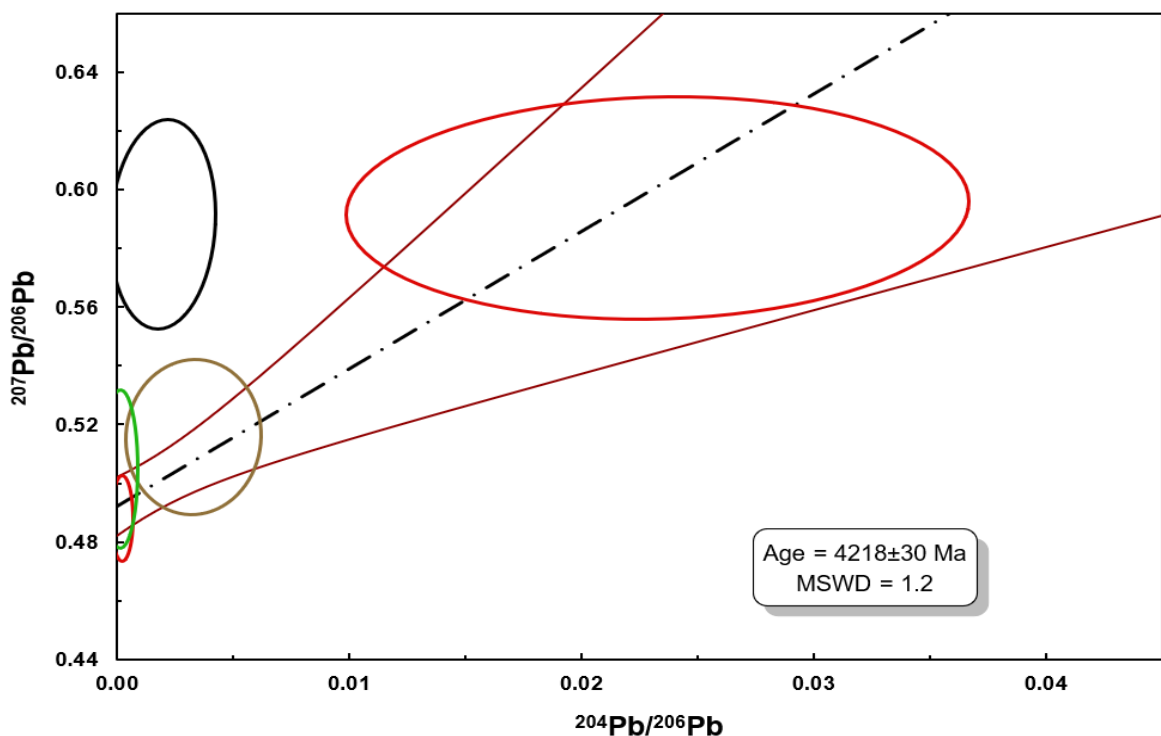


Figure 29. A reverse Pb/Pb isochron of phosphates located in clasts C3 (yellow), C4 (black), C5 (green), and the matrix (red). Clast C4 was not used in regressions. Data from clasts C3, C5 and the matrix appear to define an intercept $^{207}\text{Pb}/^{206}\text{Pb} = 0.4922 \pm 0.010$, age = 4218 ± 30 Ma, MSWD = 1.2. Clast C4 does not lie on any data array and represents a single data point from a fine-grained clast. The age corresponding to its measured $^{207}\text{Pb}/^{206}\text{Pb} = 4479 \pm 71$ Ma.

texture and age than the rest of the sample. Clast C4 has a more fine-grained basaltic texture when compared to the other clasts in LEW 85300,46. C4 also has a much older age (4479 ± 71 Ma) than the rest of the clasts, so this clast is likely recording an older metamorphic event.

	Phos 11	Phos 12a	Phos 12b	Phos 13	Phos 16	Phos 21	Phos 22	Phos 24	Phos 25
	C1	C1	C1	C1	C1	C5	C3	C4	M
La	99.0	90.2	87.4	78.0	82.1	49.6	8000	64.2	62.6
Ce	317	259	219	302	216	159	21129	169	238
Pr	54.9	46.1	42.0	42.7	43.0	27.9	2906	31.2	45.7
Nd	295	257	182	221	199	139	14723	166	241
Sm	89.8	79.6	60.0	69.6	65.5	46.8	4161	51.9	75.2
Eu	1.20	1.72	2.02	2.35	1.57	1.63	32.90	3.45	1.69
Gd	107	104	72.2	79.6	75.4	48.9	4720	47.1	85.9
Tb	17.0	17.9	13.9	13.7	12.9	8.51	788	8.45	13.8
Dy	105	121	87.5	84.5	86.6	53.0	5149	54.9	86.8
Ho	19.7	21.9	18.5	16.8	16.3	10.2	1029	9.71	17.0
Er	45.0	56.3	42.3	40.1	37.3	24.2	2448	25.0	39.6
Tm	5.48	6.54	5.47	5.17	4.72	2.93	340	3.65	5.00
Yb	26.6	38.1	37.1	25.1	26.8	16.2	1787	20.0	26.1
Lu	3.03	4.44	4.23	3.08	2.95	1.68	206	2.51	2.83
Th	35.2	66.4	47.2	32.2	25.8	24.1	1230	74.1	64.6
U	150	182	131	163	108	116	143	170	147

Table 2. This table is the trace element concentrations (ppm) of the phosphate minerals that were measured in figure 29. The different phosphates are categorized, and color coded based on their location. clast C1 is blue, clast C3 is yellow, clast C4 is black, clast C5 is green, and the matrix (abbreviated to M) is red. Phosphates 1-10 are not included in the REE table due to lab restrictions during the COVID-19 lockdown. Unfortunately, this does include phosphates 4a, 4b, 5a, and 5b, which were the only phosphates found within clast C2.

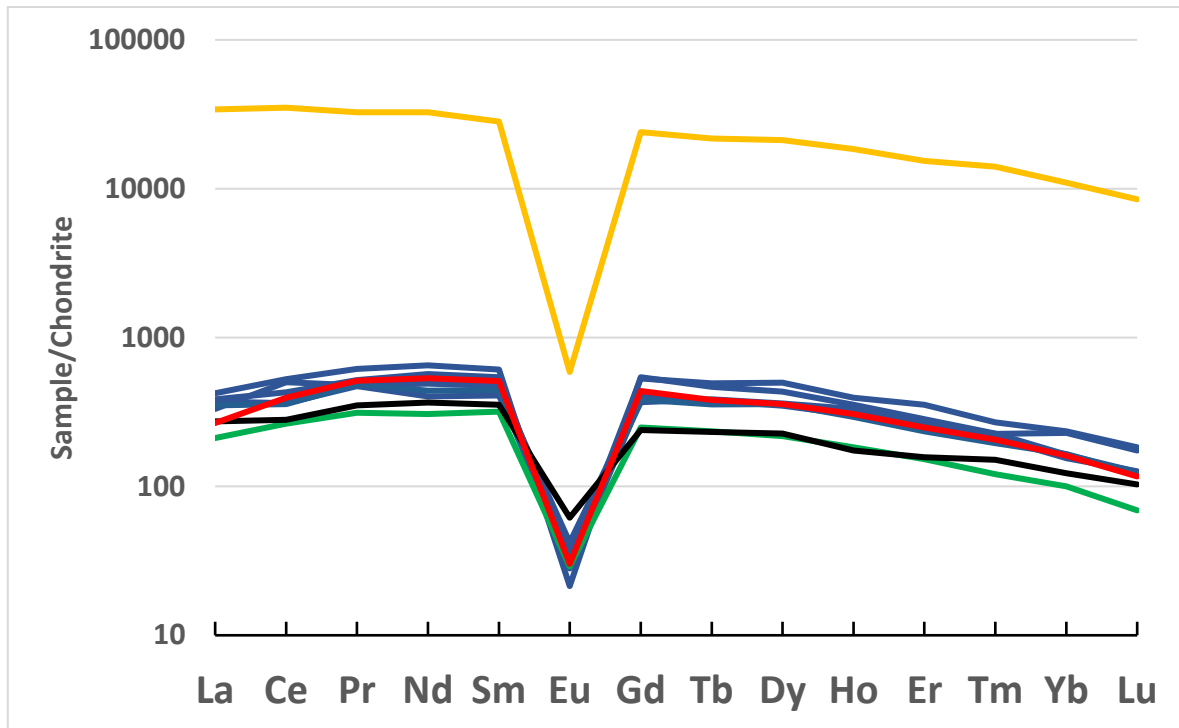


Figure 30. A rare-earth element graph of phosphates 11, 12a, 12b, 13, 16, 21, 22, 24, and 25. The different colors on the graph corresponds to the clast/ matrix that the phosphate was found in. Clast C1 is blue, C3 is yellow, C4 is black, C5 is green, and the matrix is red. The yellow phosphate from clast C3 is a merrillite, and the other phosphates from clasts C1, C4, and matrix are all apatites. Phosphates 1-10 do not have any REE data due to lab restrictions during the COVID-19 lockdown.

5. Discussion

5.1 Three ages of LEW 85300,46

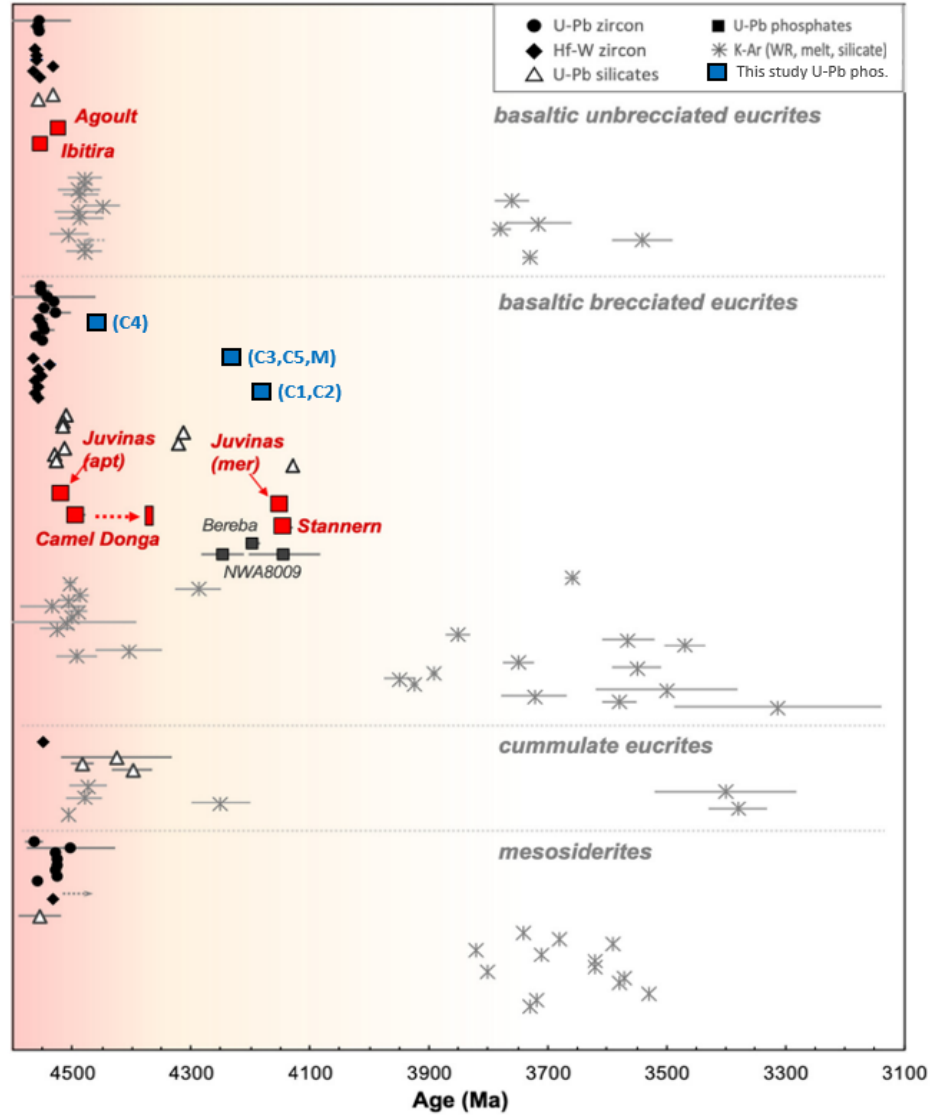


Figure 31. A compilation of ages from (Koike et al. 2020) with the addition of the ages from LEW 85300,46 with 2 standard deviations of error. The graph is separated into four different sections based on the categories of meteorites tested. LEW 85300,46 is a brecciated polymict eucrite, so it's been placed in the basaltic brecciated eucrite category.

LEW 85300,46 contains 3 distinct ages of U-Pb in phosphate. The first is the 4126 ± 18 Ma age found in the gabbroic clasts, C1 and C2. The second is the 4218 ± 30 Ma age found in the smaller clasts, C3, C5, and matrix. The third is the 4479 ± 71 Ma age found in the fine grained, basalt clast C4. This age only comes from a single phosphate and isn't included in the linear regressions in figures 8 or 9. All ages are plotted on figure 31.

5.2 Meaning of phosphate ages

The different U-Pb ages found in LEW 85300,46 are between other ages found using different chronometers on LEW 85300. The Ar-Ar ages of LEW 85300,55 give an age of ~ 3500 Ma, while the whole-rock Rb-Sr ages of LEW85300,55 give an age of ~ 4560 Ma (Nyquist et al. 1990). The oldest ages on Vesta are found in zircons and represent some of the initial crystallization age of eucrites ~ 4560 (Iizuka et al. 2015). Resetting of the U-Pb system in phosphate after crystallization likely occurred from major impacting and post-impact ejecta blanket heating. These events are recorded in the U-Pb phosphate ages found in LEW 85300,46 that span from 4479 to 4126 Ma, during a period of relatively few Ar-Ar ages (Figure 31).

5.3 Timeline from isotope ages

Isotope ages from different systems can be broken down into groups of three different ages. The first is the initial crystallization of 4-Vesta. Second, is the initial burst of high impact frequency or velocity. Finally, there is the “tail end” of impacting, where the number of impacts decreased, the velocity of impacts decreased, or both decreased (Koike et al. 2020). The initial crystallization ages of the HED parent body are preserved in the isotope systems with the highest closing temperatures, like U-Pb in zircon. These ages represent the initial crystallization, shortly

after CAI formation at ~4560 (Iizuka et al. 2015; Liao and Hsu 2017; Koike et al. 2020). After initial magma ocean crystallization and subsequent magmatism, there appears to be a volatile time in solar system history where impacting was a dominant process of parent body modification.

The U-Pb ages which have been the focus of more recent studies (Koike et al. 2020; Martinez et al. 2021) show evidence for high-energy impacts earlier in Vesta's life. Heavy impacting that occurred from ~4500 – 4100 Ma is preserved in the U-Pb system within phosphates; however, these data are sparse compared to the number of Ar-Ar data. The resetting of the U-Pb system in phosphate allows for a period of high-energy impacts to be recorded. These impacts were energetic enough to cause the HED materials to reach temperatures that would reset both the U-Pb and Ar-Ar systems. This event is what is now being referred to as an “early bombardment” (Koike et al 2020). The ages found in LEW 85300,46 (4126 ± 18 Ma, 4218 ± 30 Ma, and 4479 ± 71 Ma) are recording this “early bombardment” or EB, that took place prior to 4.1 Ga. Other recent studies have shown similar results, such as the apatites in Juvinas with a $^{207}\text{Pb}/^{206}\text{Pb}$ age of 4150.3 ± 11.6 Ma (Koike et al. 2020 and references therein). Phosphates in the diogenite NWA 10666 have a U-Pb age of 4248 ± 25 Ma (Martinez et al. 2021).

After 4.1 Ga there is what is traditionally known as the “late heavy bombardment” or LHB. There is new evidence that shows that the LHB may actually represent the waning stages of inner Solar System impacting. The ‘LHB’ impacting was energetic enough to reset the Ar-Ar but not the U-Pb decay systems in phosphate, which have closure temperatures of ~300°C and ~550°C, respectively (Cherniak and Watson 2001). Thus, these data are consistent with, at least at a large

scale, models of progressively waning impact intensity during a period from 4500-3300 Ma (e.g., Koike et al., 2020) instead of a pronounced bombardment between 3800 and 3300 (e.g., Cohen 2013).

Figure 32 shows hypothetical impact curves for Vesta. The blue curve is a linear curve, where the impact flux of Vesta is steadily decreasing over time. The second is the red curve which shows an exponential decay of impact flux. Finally, the green curve shows a curve where the impacts are exponentially decreasing, but then experience a secondary increase in impacting near 3.5Ga. These curves are hypothetical and further testing is necessary to determine what the actual impact flux curve of Vesta looks like.

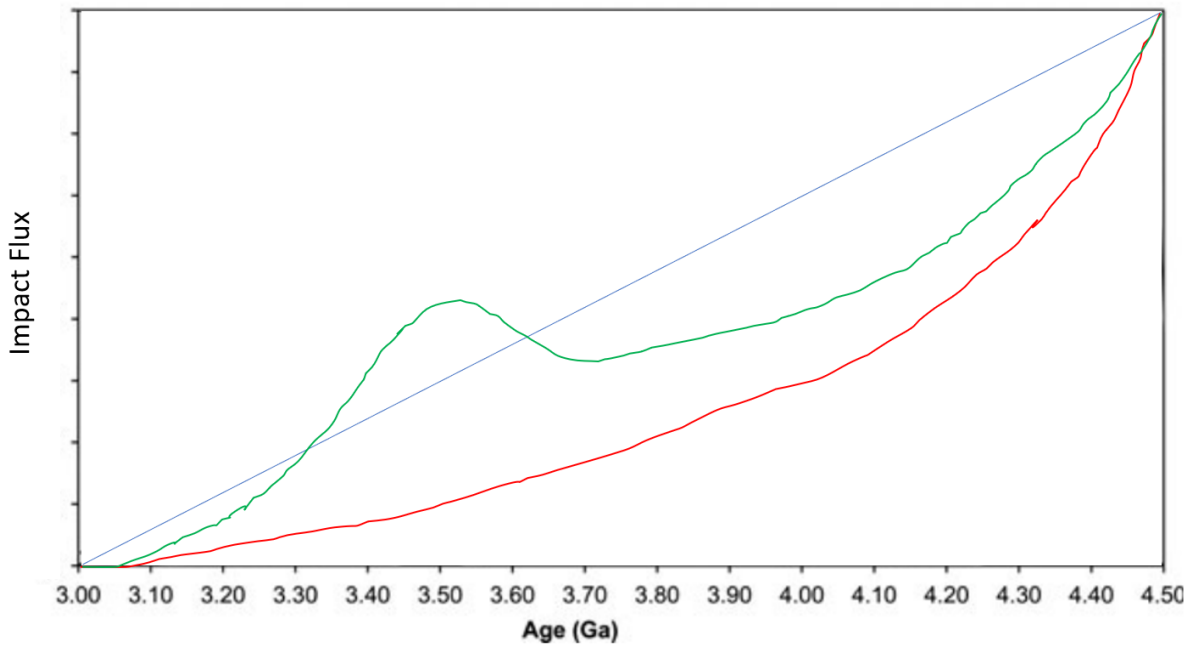


Figure 32. This is an estimation for what different impact flux curves might look like for Vesta.

6. Conclusion

Phosphates in polymict eucrite LEW 85300,46 were analyzed for their Pb isotope compositions and trace element geochemistry. Three distinct phosphate ages were found in distinct clasts and matrix within LEW 85300,46 (4479 ± 71 Ma, 4218 ± 30 Ma, 4126 ± 18 Ma). These ages correspond to a period of time between 4.5 and 4.1 Ga which predates the hypothesized LHB. The U-Pb in phosphate ages likely record intense impact metamorphism that is not typically recorded by the Ar-Ar system. Therefore, it is possible that the inner solar system did not experience a LHB, but instead experienced progressively waning impact intensity.

Bibliography

Amelin Y., Krot A. N., Hutcheon I. D., Ulyanov A. A. (2002) Lead Isotopic Ages of Chondrules and Calcium-Aluminum-Rich Inclusions. *Science* **297**, 1678-1683.

Barfod G. H., Krogstad E. J., Frei R., Albarede F. (2005) Lu-Hf and PbSL geochronology of apatites from Proterozoic terranes: A first look at Lu-Hf isotopic closure in metamorphic apatite. *Geochimica et Cosmochimica Acta* **69**, 1847-1859.

Beck, A.W., McSween Jr., H.Y., (2010) Diogenites as polymict breccias composed of orthopyroxenite and harzburgite. *Meteoritics & Planetary Science* **45**, 850–872.

Bogard D. D. (1995) Impact ages of meteorites: a synthesis. *Meteoritics & Planetary Science* **30**, 244-268.

Bogard D. D. and Garrison D. H. (1995) ^{39}Ar - ^{40}Ar Age of the Ibitira Eucrite and Constraints on the Time of Pyroxene Equilibration. *Geochimica et Cosmochimica Acta* **59**, 4317-4322.

Bogard D. D. and Garrison D. H. (2003) ^{39}Ar - ^{40}Ar ages of eucrites and thermal history of asteroid 4 Vesta. *Meteoritics and Planetary Science* **38**, 669–710.

Bouvier A., Blichert-Toft J., Moynier F., Vervoort F. A. (2007) Pb-Pb Dating Constraints on the Accretion and Cooling History of Chondrites. *Geochimica et Cosmochimica Acta* **71**, 1583-1604.

Cherniak D. J. and Watson E. B. (2001) Pb Diffusion in Zircon. *Chemical Geology* **172**, 5-24.

Cohen B. A. (2013) The Vestan cataclysm: Impact-melt clasts in howardites and the bombardment history of 4 Vesta. *Meteoritics & Planetary Science* **48**, 771-785.

Deidterich J. E. (2012) Isotope Systematics of the Eucrite Jonzac: A look into the Eucrite Parent Body Using the Lu-Hf, Sm-Nd, Pb-Pb, and U-Pb Isotope Systems. MSc Thesis. University of Houston.

Dominik C., Tielens A. G. G. M. (1997) The Physics of Dust Coagulation and the Structure of Dust Aggregates in Space. *The Astrophysical Journal* **480**, 647-673.

Dreibus G., Wanke H. (1980) The Bulk Composition of the Eucrite Parent Asteroid and its Bearing on Planetary Evolution. *Zeitschrift fur Naturforschung* **35a**, 204-216.

Duke, M.B., Silver, L.T. (1967) Petrology of eucrites, howardites and mesosiderites. *Geochimica et Cosmochimica Acta* **31**, 1637-1665.

Gomes R., Levison H. F., Tsiganis K., Morbidelli A. (2005) Origin of the cataclysmic late heavy bombardment period of the terrestrial planets. *Nature* **435**, 466-469.

Greenwood R. C., Franchi I. A., Jambon A., Barrat J. A. and Burbine T. H. (2006) Oxygen Isotope Variation in Stony-Iron Meteorites. *Science* **313**, 1763-1765.

Hopkins M. D., Mojzsis S. J., Bottke W. F., Abramov O. (2015) Micrometer-scale U-Pb age domains in eucrite zircons, impact re-setting, and the thermal history of the HED parent body. *Icarus* **245**, 367-378.

Iizuka T., Yamaguchi A., Haba M. K., Amelin Y., Holden P., Zink S., Huyskens M. H., Ireland T. R. (2015) Timing of global crustal metamorphism on Vesta as revealed by

high-precision U-Pb dating and trace element chemistry of eucrite zircon. *Earth and Planetary Science Letters* **409**, 182–192.

Iizuka T., Jourdan F., Yamaguchi A., Koefoed P., Hibiya Y., Ito K. T M., Amelin Y. (2019) The geologic history of Vesta inferred from combined $^{206}\text{Pb}/^{207}\text{Pb}$ and $^{40}\text{Ar}/^{39}\text{Ar}$ chronology of basaltic eucrites. *Geochimica et Cosmochimica Acta*. **267**, 275-299.

Jérome, D.Y., Goles, G.G., (1971) A re-examination of relationships among pyroxene-plagioclase achondrites. In: Brunfelt, A.O., Steinnes, E. (Eds.), *Activation Analysis in Geochemistry and Cosmochemistry*. Universitetsforlaget, Oslo, pp. 261–266.

Kennedy T., Jourdan F., Eroglu E., Mayers C. (2019) Bombardment history of asteroid 4 Vesta recorded by brecciated eucrites: large impact event clusters at 4.50 Ga and discrete bombardment until 3.47 Ga. *Geochimica et Cosmochimica Acta*. **260**, 99-123.

Kleine T., Touboul M., Bourdon B., Nimmo F., Mezger K., Palme H., Jacobsen S. B., Yin Q. Z., Halliday A. N. (2009) Hf-W Chronology of the Accretion and Early Evolution of Asteroids and Terrestrial Planets. *Geochimica et Cosmochimica Acta*, **73**, 5150-5188.

Koike M., Sano Y., Takahata N., Iizuka T., Ono H., Mikouchi T. (2020) Evidence for Early Asteroidal Collisions Prior to 4015 Ga from Basaltic Eucrite Phosphate U-Pb Chronology. *Earth and Planetary Science Letters* **549**, 116497.

Kozul J., and Hewins R. H. (1988) LEW 85300,02,03 Polymict Eucrite Consortium—I: Petrology of Igneous Clasts. *19th Lunar and Planetary Science Conference*, Abstract #1324.

Kozul J., and Hewins R. H. (1988) LEW 85300,02,03 Polymict Eucrite Consortium—II: Breccia Clasts, CM Inclusion, Glassy Matrix and Assembly History. *19th Lunar and Planetary Science Conference*, Abstract #1325.

Liao S. and Hsu W. (2017) The petrology and chronology of NWA 8009 impact melt breccia: Implication for early thermal and impact histories of Vesta. *Geochimica et Cosmochimica Acta*. **204** 159-178.

Mandler B. E., Elkins-Tanton L. T. (2013) The Origin of Eucrites, Diogenites, and Olivine Diogenites: Magma Ocean Crystallization and Challow Magma Chamber Processes on Vesta. *Meteoritics and Planetary Science* **48**, 2333-2349.

Marchi S., McSween H. Y., O'Brien D. P., Schenk P., De Sanctis M. C., Gaskell R., Jaumann R., Mottola S., Preusker F., Raymond C. A., Roatsch T., and Russell C. T. (2012) The violent collisional history of asteroid 4 Vesta. *Science* **336**, 690-694.

Martinez C., Lapen T. J., Richter M., Irving A. J. (2020) Petrologic Characterization and U-Th-Pb Chronology of Ca-Phosphate in Noritic Diogenite Northwest Africa 10666. *51st Lunar and Planetary Science Conference*, Abstract #2710.

McCord, T.B., Adams, J.B., Johnson, T.V., (1970) Asteroid Vesta: Spectral Reflectivity and Compositional Implications. *Science* **168**, 1445–1447.

McSween H. Y., Binzel R. P., De Sanctis M. C., Ammannito E., Prettyman T. H., Beck A. W., Reddy V., Le Corre L., Gaffey M. J., McCord T. B., Raymond C. A., Russell C. T., The Dawn Science Team. (2013) Dawn; the Vesta-HED connection; and the geologic

context for eucrites, diogenites and howardites. *Meteoritics & Planetary Science* **48**, 2090-2104.

Melosh H. J. (1989) Geologic Collisions: Impact Cratering. A Geological Process. *Science* **245**, 1261-1262.

Misawa K., Yamaguchi A., Kaiden H. (2005) U-Pb and ^{207}Pb - ^{206}Pb Ages of Zircons from Basaltic Eucrites: Implications for Early Basaltic Volcanism on the Eucrite Parent Body. *Geochimica et Cosmochimica Acta* **69**, 5847-5861.

Mittlefehldt D. W., McCoy T. J., Goodrich C. A., Kracher A. (1998) Non-Chondritic Meteorites from Asteroidal Bodies. *Reviews in Mineralogy and Geochemistry* **36**, 1-195.

Mittlefehldt D. W., Beck A. W., Lee C. T. A., McSween H. Y., Buchanan P.C. (2012) Compositional constraints on the genesis of diogenites. *Meteoritics & Planetary Science* **47**, 72-98.

Mittlefehldt D. W., Herrin J. S., Quinn J. E., Mertzman S. A., Cartwright K. R., Peng Z. X. (2013) Composition and Petrology of HED Polymict Breccias: The Regolith of (4) Vesta. *Meteoritics and Planetary Science* **48**, 2105-2134.

Nyquist L. E., Bogard D. D., Bansal B. M., Wiesmann H., Shih C. Y. (1990) Ar-Ar, Rb-Sr, and Sm-Nd Studies of Eucrite Clast LEW85300,55. *21st Lunar and Planetary Science Conference*, Abstract #1459.

Nyquist L. E., Reese Y., Wiesmann H., Shih C. Y. (2001) Age of EET79001B and Implications for Shergottite Origins. *32nd Lunar and Planetary Science Conference*, Abstract #1407.

Pfalzner S., Davies M. B., Gounelle M., Johansen A., Münker C., Lacerda P., Portegies-Zwart S., Testi L., Trialet M., Veras D. (2015) The formation of the solar system. *Physica Scripta* **90**, 1-18.

Pollack J. B., Hubickyj O., Bodenheimer P., Lissauer J. J., Podolak M., Greenzweig Y. (1996) Formation of the Giant Planets by Concurrent Accretion of Solids and Gas. *Icarus* **124**, 62-85.

Pun A., Keil K., Taylor G. J., and Wieler R. (1998) The Kapoeta howardite: Implications for the regolith evolution of the HED parent body. *Meteoritics & Planetary Science* **33**, 835–851.

Righter K., Drake M. J. (1997) A Magma Ocean on Vesta: Core Formation and Petrogenesis of Eucrites and Diogenites. *Meteoritics and Planetary Science* **32**, 929-944.

Robertson A. P., Righter M., Lapen T. J. (2020) 4.137 Ga Metamorphic age for polymict eucrite LEW85300. *51st Lunar and Planetary Science Conference*, Abstract #2836.

Ruzicka A., Snyder G. A., Taylor L. A. (1997) Vesta as the Howardite, Eucrite and Diogenite Parent Body: Implications for the Size of a Core and for Large-Scale Differentiation. *Meteoritics and Planetary Science* **32**, 825-840.

Safronov V. S., Zvjagina E. V. (1969) Relative Sizes of the Largest Bodies During the Accumulation of Planets. *Icarus* **10**, 109-115.

Schiller M., Baker J. A., Bizzarro M. (2010) ^{26}Al - ^{26}Mg Dating of Asteroidal Magmatism in the Young Solar System. *Geochimica et Cosmochimica Acta* **74**, 4844-4864.

Schmitz M. D., Schoene B. (2007) Derivation of isotope ratios, errors and error correlations for U-Pb geochronology using ^{205}Pb - ^{235}U -(^{233}U)-spiked isotope dilution thermal ionization mass spectrometric data. *Geochemistry, Geophysics, Geosystems* **8**, 1-20.

Sears D. W. G., Symes S. K. J., Batchelor J. D., Akridge D. G., Benoit P. H. (1997) The metamorphic history of eucrites and eucrite-related meteorites and the case for late metamorphism. *Meteoritics & Planetary Science* **32**, 917-927.

Shu F. H., Adams F. C., Lizano S. (1987) Star Formation in Molecular Clouds: Observation and Theory. *Annual Review of Astronomy and Astrophysics* **25**, 23-81.

Tera F., Carlson R. W., Boctor N. Z. (1997) Radiometric ages of basaltic achondrites and their relation to the early solar system. *Geochimica et Cosmochimica Acta* **61**, 1713-1731.

Thompson S. N., Gehrels G. E., Ruiz J., Buchwaldt R. (2012) Routine Low-Damage Apatite U-Pb Dating Using Laser Ablation-Multicollector-ICPMS. *Geochemistry, Geophysics, Geosystems* **13**, 1-23.

Trinquier A., Birck J. L., Allegre C. J., Gopel C., Ulfbeck D. (2008) ^{53}Mn - ^{53}Cr Systematics of the Early Solar System Revisited. *Geochimica et Cosmochimica Acta*, **72**, 5146-5163.

Tsiganis, K., Gomes, R., Morbidelli, A. & Levison, H. F. (2005) Origin of the orbital architecture of the giant planets of the Solar System. *Nature* **435**, 459-461.

Warren P. H., Kallemeyn G. W., Huber H., Ulf-Møller F., Choe W. (2009) Siderophile and other geochemical constraints on mixing relationships among HED-meteoritic breccias. *Geochimica et Cosmochimica Acta* **73**, 5918-5943.

Wurm G., Paraskov G., Krauss O. (2005) Growth of Planetesimals by Impacts at ~25m/s. *Icarus* **178**, 253-263.

Zhang C., Miao B., He H. (2019) Oxygen isotopes in HED meteorites and their constraints on parent asteroids. *Planetary and Space Science* **168**, 83-94.

Zolensky M. E., Hewins R. H., Mittlefehldt D. W., Lindstrom M. M., Xiao X., Lipschutz M. E. (1992) Mineralogy, Petrology, and Geochemistry of Carbonaceous Chondrite Clasts in the LEW 85300 polymict eucrite. *Meteoritics and Planetary science* **27**, 596-604.